Modelling adhesion and friction in contact problems

Khajeh Salehani, Mohsen

DOI
10.4233/uuid:d53f2842-480c-4cf2-b8c7-cbaf157d4398

Publication date
2019

Document Version
Final published version

Citation (APA)
Khajeh Salehani, M. (2019). *Modelling adhesion and friction in contact problems*. [Dissertation (TU Delft), Delft University of Technology]. https://doi.org/10.4233/uuid:d53f2842-480c-4cf2-b8c7-cbaf157d4398

MODELLING ADHESION AND FRICTION IN CONTACT PROBLEMS

MODELLING ADHESION AND FRICTION IN CONTACT PROBLEMS

Proefschrift

ter verkrijging van de graad van doctor
aan de Technische Universiteit Delft,
op gezag van de Rector Magnificus prof. dr. ir. T.H.J.J. van der Hagen,
voorzitter van het College voor Promoties,
in het openbaar te verdedigen op
Dinsdag 9 juli 2019 om 12:30 uur

door

Mohsen KHAJEH SALEHANI

Master of Science in Computational Solid Mechanics,
Sharif University of Technology, Iran
geboren te Teheran, Iran.

Dit proefschrift is goedgekeurd door de promotoren.

Samenstelling promotiecommissie:

Rector Magnificus,	voorzitter
Prof. dr. ir. L. Nicola	Technische Universiteit Delft, promotor
Dr. N. Irani	Technische Universiteit Delft, copromotor
Onafhankelijke leden:	
Prof. dr. ir. J. Sietsma	Technische Universiteit Delft
Prof. dr. I.M. Richardson	Technische Universiteit Delft
Prof. Ing. G. Carbone	Politecnico di Bari, Italië
Dr. J. Scheibert	École Centrale de Lyon, Frankrijk
Dr. ir. M. van Drogen	DAF Trucks N.V.

This research was carried out at Delft University of Technology and was funded by the Netherlands Organisation for Scientific Research NWO (VIDI grant 12669).

Keywords: Tribology, Adhesion and Friction, Contact Area and Load, Rough Surfaces, Green's Function Molecular Dynamics, Cohesive Law

Printed by: ProefschriftMaken || www.proefschriftmaken.nl

Cover: The difference between adhesive and non-adhesive contact. Colour code: black (self-affine rough rigid profile), green (deformed configuration in adhesive contact), and red (deformed configuration in non-adhesive contact).

ISBN 978-94-6380-408-0

An electronic version of this dissertation is available at
http://repository.tudelft.nl/.

To all the kind hearts, the brilliant minds, and the brave souls

CONTENTS

SUMMARY

The main objective of this thesis is to obtain a better understanding of adhesive contacts and their frictional behaviour. Both natural and man-made surfaces are rough over a wide range of length scales. Tribological studies of rough surfaces need to account for the interactions between these asperities. In this work a simple atomistically–inspired macro-scale model is developed to study smooth and rough contacts between elastically deformable bodies where adhesion and friction are simultaneously active at the interface.

A full description of the model is presented in Chapter 2. There, the Green's function molecular dynamics (GFMD) technique is extended to explicitly describe the two solids in contact and their mixed-mode interface interactions. The interactions between surfaces are described through a coupled cohesive-zone model implemented in the GFMD technique. The extended GFMD technique includes an incremental iterative scheme, which is necessary to capture the contact area evolution when tangential tractions develop at the interface between the solids under loading.

In Chapter 3 the non-adhesive contact between a rigid rough indenter and an incompressible elastic solid is studied. It is shown that for rough line contacts, only when the root-mean-square gradient is calculated over the *actual* contact area a linear relation exists between the relative contact area and the reduced pressure, such that the proportionality factor is independent of Hurst exponent and reduced pressure. Moreover, based on the obtained values for the proportionality factor in line (1D) and surface (2D) contacts, a single 1D-to-2D scaling factor is found for both rough and smooth non-adhesive asperities.

Next, with the aim of capturing the consequences of the interplay between adhesion and friction, contact of a periodic array of smooth circular rigid asperities indenting into a flat deformable solid is studied in Chapter 4. It is shown that for a given normal work of separation, the contact size and the pull-off load increase by increasing friction. However, the interplay between adhesion and friction can be neglected in all cases where relative sliding of the surfaces is small, i.e. when one of these three conditions hold: (1) friction is very large, (2) the material is incompressible, (3) contacts are closely spaced.

In Chapter 5 the adhesive contact of a self-affine rough rigid solid indenting

an initially flat deformable solid is analysed. It is shown that, unlike the non-adhesive contacts, the relation between the relative contact area and the reduced pressure has a non-linear behaviour in the case of adhesive contact, particularly for rough profiles with large Hurst exponent and small root-mean-square height. However, it is found that for the indentation of a self-affine rough rigid profile, frictional property of the interface as well as compressibility of the substrate becomes irrelevant to the load-area relation, due to the interference of the displacement fields of the neighbouring asperities on various length scales.

Contact problems that include also tangential loading are studied in Chapter 6, where a mixed normal and tangential loading is applied. Simulations are performed for the frictional sliding of the adhesive contact between a circular smooth punch against a flat rigid substrate, under tension and compression. It is shown that with slip instabilities occurring during sliding, a cycle of contact area reduction and reattachment persists for continued tangential loading, even under tension. Whether the reattachment is partial or full depends on friction: The lower the friction, the more complete the reattachment. Moreover, the reduction in the contact area as a function of the tangential contact force is found to be well fitted by the empirical quadratic law reported from experimental results under compressive loading. Under tensile loading, however, the quadratic law breaks down: There is a larger rate of contact area reduction when the onset of sliding is approached.

SAMENVATTING

Het voornaamste doel van dit proefschrift is het verkrijgen van een beter inzicht in adhesieve contacten en hun wrijvingsgedrag. Zowel natuurlijke als artificiële oppervlakken zijn ruw over een groot aantal lengteschalen. Voor tribologisch onderzoek naar ruwe oppervlakken is het noodzakelijk om de interactie tussen uitsteeksels mee te nemen. In dit werk is een eenvoudig, door atomistische modellen-geïnspireerd, macroschaal model ontwikkeld om gladde en ruwe contacten tussen elastisch vervormbare lichamen te bestuderen, waarbij adhesie en wrijving gelijktijdig aan het interface voorkomen.

Een volledige beschrijving van het model wordt gegeven in Hoofdstuk 2. De Green's functie moleculaire dynamica (GFMD) methode is uitgebreid om expliciet de twee vaste stoffen in contact en hun mixed-mode interface-interactie te beschrijven. De interacties tussen de oppervlakken worden beschreven door een gekoppeld cohesieve-zone-model dat is geïmplementeerd in de GFMD methode. In de uitgebreide GFMD methode is een incrementeel iteratief schema opgenomen. Dit is noodzakelijk voor het beschrijven van de contactevolutie wanneer tangentiële krachten ontwikkelen aan het interface tussen de vaste stoffen die in contact met elkaar zijn.

In Hoofdstuk 3 wordt het non-adhesievie contact tussen een rigide ruwe indenter en een onsamendrukbare elastische vaste stof bestudeerd. Het blijkt dat alleen wanneer de kwadratisch gemiddelde gradiënt is berekend over het echte contactoppervlak, er voor ruwe lijncontacten een lineaire relatie tussen het relatieve contactoppervlak en de gereduceerde druk bestaat, zodat de proportionaliteitsfactor onafhankelijk is van de Hurst-exponent en de gereduceerde druk. Bovendien, gebaseerd op de verkregen waarden voor de proportionaliteitsfactor voor lijn- (1D) en oppervlak- (2D) contacten, een enkelvoudige 1D-naar-2D schaalfactor is gevonden voor zowel ruwe als gladde non-adhesieve uitsteeksels.

Vervolgens, met het doel om de gevolgen van het samenspel tussen adhesie en wrijving te beschrijven, wordt het contact tussen een periodieke array van gladde circulaire rigide uitsteeksels die in een vlak vervormbare vaste stof drukken, bestudeerd in Hoofdstuk 4. Er wordt getoond dat voor een gegeven benodigde arbeid voor separatie, de contactgrootte en de aftrekbelasting toenemen door toenemende wrijving. Echter, het samenspel tussen adhesie en wrijving

kan worden verwaarloosd in alle gevallen waar het relatieve glijden van de oppervlakken klein is, d.w.z. wanneer aan één van deze drie voorwaarden voldaan wordt: (1) wrijving is zeer groot, (2) het materiaal is onsamendrukbaar, (3) contacten zijn nauw opeenvolgend.

In Hoofdstuk 5 wordt het adhesieve contact van een zelf-affiene ruw rigide vaste stof die in een initieel vlak vervormbare vaste stof drukken, geanalyseerd. Er wordt getoond dat, in tegenstelling tot non-adhesieve contacten, de relatie tussen het relatieve contactoppervlak en de gereduceerde druk een non-lineair gedrag heeft voor het geval van adhesieve contacten, in het bijzonder voor ruwe profielen met een hoge Hurst-exponent en een kleine kwadratisch gemiddelde hoogte. Echter, voor de indeuking van een zelf-affiene ruw rigide profiel is gevonden dat de wrijvingseigenschap van het interface en de compressibiliteit van het substraat relevant worden in de belasting-contact-relatie door de interferentie van de verplaatsingsvelden van naastliggende uitsteeksels op verschillende lengteschalen.

Contactproblemen aangaande tangentiële belasting zijn in Hoofdstuk 6 bestudeerd, waar een gemengde normale en tangentiële belasting is toegepast. Simulaties zijn uitgevoerd voor wrijvend glijden van het adhesieve contact tussen een circulaire gladde indenter op een vlak rigide substraat onder rek en compressie. Er wordt getoond dat met glij-instabiliteiten tijdens het glijden een cyclus van contactoppervlakreductie en herbevestiging aanhoudt voor continuering van tangentiële belasting, zelf tijdens rek. Of de herbevestiging deels of volledig is hangt af van de wrijving: Hoe kleiner de wrijving, hoe completer de herbevestiging. De reductie van het contactoppervlak als functie van de tangentiële kracht blijkt goed beschreven met een empirische kwadratische wet gevonden in experimenten onder compressieve belasting. Echter, onder rekbelasting is de kwadratische wet niet toepasbaar: Er is een grotere snelheid van contactoppervlakreductie wanneer het begin van glijden wordt benaderd.

1

INTRODUCTION

The improvement of understanding is for two ends:
first, our own increase of knowledge;
secondly, to enable us to deliver
that knowledge to others.

John Locke

1

1.1. GENERAL INTRODUCTION

THE importance of friction cannot be overestimated, as it affects everyday life in countless situations. Friction is either desired or detrimental depending on the application: In the absence of friction, for example, one would not be able to play the violin or even turn to the next page while reading this thesis. However, friction by resisting the relative motion of contacting bodies, is also a source of energy dissipation and responsible for a third of the world energy consumption [1]. This "double-edged sword" behaviour of friction goes hand in hand with the complex nature of this phenomenon.

The surface topography and its adhesive properties influence their contact and frictional behaviour. Thus, a rigorous understanding of how roughness and adhesion affect the contact behaviour of materials is of great importance and is the main focus of this thesis.

Despite the great advances made in recent years, the understanding of friction relies highly on Amontons' law which states that for any two materials the friction force is directly proportional to the normal load. The common interpretation of this law is that contact area increases linearly with the applied normal load. The law is applied independently of whether the interface is adhesive or non-adhesive. With the aim of investigating the load-area evolution while considering adhesion forces at the interface, in the past decades, many attempts have been made to model adhesive contact problems under normal loading. The first adhesive contact theories to appear were the widely used theories developed by Johnson, Kendall, and Roberts (JKR) [2] for short-range adhesion and by Derjaguin, Muller, and Toporov (DMT) [3] for long-range adhesion in a Hertzian contact geometry. More recently, Borodich *et al.* [4] have extended the analytical JKR theory and studied the adhesive contact under both frictionless and full stick boundary conditions. The idea that adhesion and friction affect each other is generally attributed to Desaguliers (1734) [5]. Bowden and Tabor (1950) [6] turned this idea into a principal part of their theory of friction, but [4] neglected the coupling between adhesion and friction. The role of this coupling in the evolution of contact area and load still needs to be well understood. In this thesis, the consequences of the interplay between adhesion and friction during contact loading are investigated.

Beyond contact problems under pure normal loading, in the seminal work by Savkoor and Briggs [7] mixed normal and tangential loading was applied to a rubber hemisphere in adhesive contact with a glass plate. It was found that as a result of increasing the tangential load, the surfaces tend to peel apart and hence, the contact area decreases progressively. Later, Waters and Guduru [8] and more

recently Sahli *et al.* [9] performed similar experiments and demonstrated that there is indeed a contact area reduction during shear loading. With the aim of reproducing the experimental results, adhesive contacts under mixed-mode loading have been extensively studied in [5, 7, 8, 10–15]. However, these studies are limited to investigating the contact area evolution either up to the onset of sliding or only under compressive loading. The contact evolution after the onset of sliding and under tensile loading, however, has not yet been addressed. In this thesis, a complete picture of contact evolution of an adhesive circular smooth punch under mixed-mode loading, before and after sliding, is provided.

1.2. OBJECTIVE AND OUTLINE OF THE THESIS

The main objective of this thesis is to obtain a better understanding of adhesive contacts and their frictional behaviour. To this end, a simple atomistically-inspired macro-scale model is developed in order to study smooth and rough contacts between elastically deformable bodies where adhesion and friction are simultaneously active at the interface.

In Chapter 2 the atomistically-inspired contact model is presented. Thereafter, this model is employed to investigate the contact evolution under various loadings. This investigation is categorized into two parts. In Part I, indentation contact problems under single–mode (pure normal) loading are studied. This part is divided into three chapters, depending on the interface property (non-adhesive or adhesive) and surface topography (smooth or rough).

In Chapter 3 the non-adhesive contact between a rigid indenter and an incompressible elastic solid is studied. In this chapter, the assumption of linearity between contact area and applied normal load for random rough and smooth asperities is assessed in line (1D) and surface (2D) contacts.

In Chapter 4 the analysis in Chapter 3 is extended to the more complicated case of adhesive contacts. Simulations are performed for a periodic array of smooth circular rigid asperities indenting a flat deformable solid, in order to evaluate the dependency of contact size, load-displacement curve, and pull-off load on the interface properties, particularly the interplay between adhesion and friction.

As the last chapter of Part I, adhesive contact of a self-affine rough rigid solid indenting an initially flat deformable solid is analysed in Chapter 5. The aim of this chapter is to investigate how adhesion contributes to the experimentally observed non-linear relation between contact area and load. Moreover, new insights are provided into the role of roughness parameters (root-mean-square height, Hurst exponent, and small wavelengths) on the evolution of contact area

with load.

In Part II contact problems beyond pure normal loading are studied, where a mixed normal and tangential loading is applied. First, the contact model introduced in Chapter 2 is extended in Chapter 6 to approach contact problems under mixed-mode loading. Frictional sliding of adhesive contact of a circular smooth punch against a flat rigid substrate, under tension and compression, is investigated.

Finally, results and conclusions are summarised in Chapter 7.

REFERENCES

[1] A. Z. Szeri, *Tribology: friction, lubrication, and wear* (McGraw-Hill, 1980).

[2] K. L. Johnson, K. Kendall, and A. Roberts, *Surface energy and the contact of elastic solids,* Proceedings of the Royal Society of London A: Mathematical, Physical and Engineering Sciences **324**, 301 (1971).

[3] B. V. Derjaguin, V. M. Muller, and Y. P. Toporov, *Effect of contact deformations on the adhesion of particles,* Journal of Colloid and Interface Science **53**, 314 (1975).

[4] F. M. Borodich, B. A. Galanov, and M. M. Suarez-Alvarez, *The JKR-type adhesive contact problems for power-law shaped axisymmetric punches,* Journal of the Mechanics and Physics of Solids **68**, 14 (2014).

[5] K. L. Johnson, *Adhesion and friction between a smooth elastic spherical asperity and a plane surface,* Proceedings of the Royal Society of London A: Mathematical, Physical and Engineering Sciences **453**, 163 (1997).

[6] F. P. Bowden and D. Tabor, *The friction and lubrication of solids*, Vol. 1 (Oxford University Press, 1950).

[7] A. Savkoor and G. Briggs, *The effect of tangential force on the contact of elastic solids in adhesion,* Proceedings of the Royal Society of London A: Mathematical, Physical and Engineering Sciences **356**, 103 (1977).

[8] J. F. Waters and P. R. Guduru, *Mode-mixity-dependent adhesive contact of a sphere on a plane surface,* Proceedings of the Royal Society of London A: Mathematical, Physical and Engineering Sciences **466**, 1303 (2010).

[9] R. Sahli, G. Pallares, C. Ducottet, I. B. Ali, S. Al Akhrass, M. Guibert, and J. Scheibert, *Evolution of real contact area under shear and the value of static*

friction of soft materials, Proceedings of the National Academy of Sciences **115**, 471 (2018).

[10] C. Thornton, *Interparticle sliding in the presence of adhesion,* Journal of Physics D: Applied Physics **24**, 1942 (1991).

[11] S. Chen and T. Wang, *General solution to two-dimensional nonslipping JKR model with a pulling force in an arbitrary direction,* Journal of Colloid and Interface Science **302**, 363 (2006).

[12] M. Ciavarella, *Fracture mechanics simple calculations to explain small reduction of the real contact area under shear,* Facta Universitatis, Series: Mechanical Engineering **16**, 87 (2018).

[13] G. G. Adams, *Stick, partial slip and sliding in the plane strain micro contact of two elastic bodies,* Royal Society Open Science **1**, 140363 (2014).

[14] G.-Y. Huang and J.-F. Yan, *A mechanical model for the adhesive contact with local sliding induced by a tangential force,* Acta Mechanica Solida Sinica **30**, 369 (2017).

[15] J. C. Mergel, R. Sahli, J. Scheibert, and R. A. Sauer, *Continuum contact models for coupled adhesion and friction,* The Journal of Adhesion **0**, 1 (2018).

2

Computational Approach

It can scarcely be denied that the supreme goal of all theory is to make the irreducible basic elements as simple and as few as possible without having to surrender the adequate representation of a single datum of experience.

Albert Einstein

Parts of this chapter have been published in Tribology International **124**, 93-101 (2018) [1].

2.1. INTRODUCTION

THE aim of this chapter is to build a simple atomistically-inspired macro-scale model to predict the evolution of contact area and load, in contact problems where friction and adhesion are simultaneously active.

Interaction between adhesion and friction is studied in [2–4] by means of the simple Dugdale model (1960) and the theory of linear elastic fracture mechanics (LEFM). However, models based on LEFM have the drawback that the stresses at the edge of the contact go to infinity [5] and that they are valid only for adhesion zones that are small compared to the contact radius [6]. Recently, much attention has been devoted to macroscale continuum mechanics approaches that are inspired by nanoscale contact behaviour. Various adhesive continuum models [7–10] have been presented that employ the Lennard-Jones potential within the framework of the finite element method (FEM). These models appear to have the advantage, over molecular dynamics, that they can handle contact problems at scales larger than the nanometer scale. However, apart from the fact that small load increments and finite element discretizations are necessary to avoid ill-conditioned stiffness matrices, these models become inaccurate when adhesion is strong [10].

Here, a computational approach is proposed to study contact between elastically deformable bodies that can easily handle strong and weak adhesion coupled with friction. Calculation of deformation and stress fields in the bodies is performed using Green's function molecular dynamics (GFMD) [11, 12]. The interactions between the surfaces are modelled through a coupled cohesive-zone model (CZM). CZMs are phenomenological traction-separation laws which have been originally proposed to study cracks. Indeed, a contact problem is analogous to a fracture problem where the edge of contact area coincides with a crack.

In this work, the GFMD technique is extended to explicitly describe the two solids in contact and their mixed-mode interface interactions. This extension includes an incremental iterative scheme, which is necessary to capture the contact area evolution when tangential tractions develop at the interface between the bodies under contact loading. The scheme is applied for the first time in GFMD, but inspired by similar algorithms used in finite element modelling.

2.2. TWO–SOLID CONTACT MODEL

In the two-solid contact model using the GFMD technique, the surface of the elastic solid is first discretized with a number of equispaced grid points, which interact with each other through an effective stiffness [11]. Subsequently, the response of the material to the external loading is obtained using damped dy-

namics by only considering the interactions of the surface grid points with their degrees of freedom coupling to the external force [13]. Eventually, based on the solution for the surface, body fields are calculated by means of analytical relations [12]. Figure 2.1 gives a schematic representation of the contact problem of two elastic solids with arbitrary material properties and generic surface roughness obeying the small slope approximation. Here, the solids are taken to be

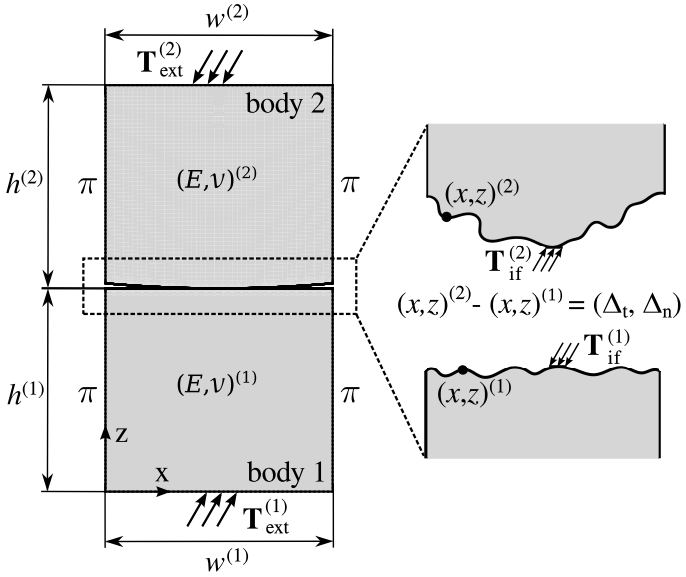

Figure 2.1: Schematic representation of two solids in contact along with the coordinate system used in the current calculations. The unit cell is periodic in x-direction, π indicates the periodic boundaries. The distance between two points on opposite surfaces is described by the gap function $g = (\Delta_t, \Delta_n)$.

elastically isotropic and plane-strain conditions are assumed with deformations restricted to the x-z plane.

The two solids under study, identified by superscript $i = \{1,2\}$, are in mechanical equilibrium at time t. Hence, the summation of the forces acting on each solid must vanish. Dividing this summation of forces by the total surface area A_0, leads to the following equilibrium equation:

$$\mathbf{T}^{(i)} = \mathbf{T}^{(i)}_{\text{el}} + \mathbf{T}^{(i)}_{\text{if}} + \mathbf{T}^{(i)}_{\text{ext}} = 0 \qquad \forall\, t, \tag{2.1}$$

where $\mathbf{T}_{\text{el}}$ is the elastic restoring force per total surface area, $\mathbf{T}_{\text{if}}$ is the interface traction and $\mathbf{T}_{\text{ext}}$ is the applied external traction. The equilibrium equations of the two solids are coupled through the action and reaction forces they exert on

each other:

$$\mathbf{T}_{\text{if}}^{(1)} = -\mathbf{T}_{\text{if}}^{(2)} \qquad \forall\, t. \tag{2.2}$$

Consequently, knowing the boundary conditions, the solution to the surface displacement fields of each solid may be obtained by solving Eq. 2.1. For the sake of simplicity, in the remaining part of this chapter, the superscript (i) is removed from the equations. All the reported relations are valid for both solids.

In the GFMD technique, due to the translational symmetry of the problem, the solution of the equilibrium equation 2.1 is obtained numerically in reciprocal space, i.e. in the Fourier representation. The main advantage of this transformation is that the non-local coupling between surface displacements and forces has a local character in reciprocal space. In order to keep track of the surface evolution during loading, the solution of Eq. 2.1 is carried out in an incremental manner [14] with the applied load increasing monotonically.

INCREMENTAL ITERATIVE SCHEME

At time t, the displacement and stress fields of the solids are known. An increment of loading $\Delta\mathbf{T}_{\text{ext}}$ is applied along the boundary $z = 0$ (for body 1) and $z = h^{(1)} + h^{(2)}$ (for body 2) and the aim is to determine the fields at time $t + \Delta t$. In reciprocal space, the equilibrium equation 2.1 is rewritten in an incremental manner as

$$\begin{aligned} \Delta\widetilde{\mathbf{T}}(q) &:= {}^{(t+\Delta t)}\widetilde{\mathbf{T}}(q) - {}^{(t)}\widetilde{\mathbf{T}}(q) \\ &= \Delta\widetilde{\mathbf{T}}_{\text{el}}(q) + \Delta\widetilde{\mathbf{T}}_{\text{if}}(q) + \Delta\widetilde{\mathbf{T}}_{\text{ext}}(q) = 0, \end{aligned} \tag{2.3}$$

where q is the wave-vector, a scalar in a 1D problem. An iterative procedure must be employed to ensure that equilibrium is satisfied at every time increment, i.e. $\Delta\widetilde{\mathbf{T}}(q) \to 0$. At iteration $m+1$, first, the estimated value of $\Delta\widetilde{\mathbf{T}}(q)$ is obtained through

$${}^{(m+1)}\Delta\widetilde{\mathbf{T}}(q) = {}^{(m+1)}\Delta\widetilde{\mathbf{T}}_{\text{el}}(q) + {}^{(m+1)}\Delta\widetilde{\mathbf{T}}_{\text{if}}(q) + \Delta\widetilde{\mathbf{T}}_{\text{ext}}(q). \tag{2.4}$$

Subsequently, the calculated value of ${}^{(m+1)}\Delta\widetilde{\mathbf{T}}(q)$ is used to modify the incremental value of the surface displacements ${}^{(m+1)}\Delta\tilde{\mathbf{u}}(q)$ through the equation of motion using the position Verlet algorithm [15]. For $m \geq 1$:

$$\begin{aligned} {}^{(m+1)}\Delta\tilde{\mathbf{u}}(q) = 2\ {}^{(m)}\Delta\tilde{\mathbf{u}}(q) - {}^{(m-1)}\Delta\tilde{\mathbf{u}}(q) \\ + \left\{ {}^{(m+1)}\Delta\widetilde{\mathbf{T}}(q) \times A_0 + \eta \left[{}^{(m)}\Delta\tilde{\mathbf{u}}(q) - {}^{(m-1)}\Delta\tilde{\mathbf{u}}(q) \right] \right\} \delta t^2, \end{aligned} \tag{2.5}$$

where η is the damping factor, δt is a pseudo time increment and

$${}^{(1)}\Delta\tilde{\mathbf{u}}(q) = {}^{(0)}\Delta\tilde{\mathbf{u}}(q) = 0. \tag{2.6}$$

The iterations in the Verlet algorithm are repeated until

$$\|^{(m+1)}\Delta\tilde{\mathbf{u}}(q) - {}^{(m)}\Delta\tilde{\mathbf{u}}(q)\| \leq \epsilon_{\mathrm{r}}, \tag{2.7}$$

where ϵ_{r} is a specified tolerance and $\|\ \ \|$ denotes the Euclidean norm. Eventually, the converged solution for ${}^{(m+1)}\Delta\tilde{\mathbf{u}}(q)$ is employed to calculate the displacement fields of the damped system at time $t + \Delta t$.

The elastic restoring force per total surface area $\widetilde{\mathbf{T}}_{\mathrm{el}}(q)$ is obtained by calculating the derivative of the elastic energy density $\widetilde{\Pi}_{\mathrm{el}}(q)$ with respect to displacement, hence,

$${}^{(m+1)}\Delta\widetilde{\mathbf{T}}_{\mathrm{el}}(q) = \frac{\partial\widetilde{\Pi}_{\mathrm{el}}(q)}{\partial\tilde{\mathbf{u}}(q)}\Big|_{{}^{(m)}\Delta\tilde{\mathbf{u}}(q)}. \tag{2.8}$$

The elastic energy density for a solid with roughness obeying the small-slope approximation is derived in [16] as

$$\widetilde{\Pi}_{\mathrm{el}}(q) = \frac{q}{2}\left[\widetilde{U}^{*}_{\alpha}(q)\right]_{1\times4}\left[\tilde{M}_{kl}(q)\right]_{4\times4}\left[\widetilde{U}_{\alpha}(q)\right]^{\mathrm{T}}_{4\times1}. \tag{2.9}$$

Here, $\widetilde{U}_{\alpha}(q)$ is given as

$$\left[\widetilde{U}_{\alpha}(q)\right] = \left[\tilde{u}_{\mathrm{x}}(q)|_{z=0} \quad \tilde{u}_{\mathrm{z}}(q)|_{z=0} \quad \tilde{u}_{\mathrm{x}}(q)|_{z=h} \quad \tilde{u}_{\mathrm{z}}(q)|_{z=h}\right], \tag{2.10}$$

where $\tilde{u}_{\alpha}$ is the displacement component of the surface grid points. The other term on the RHS of Eq. 2.9, $\tilde{M}_{kl}(q)$, depends on the stiffness tensor and on the height of the solid h:

$$\left[\tilde{M}_{kl}(q)\right] = C_{11}\begin{bmatrix} \tilde{M}_{11}(q) & -i\tilde{M}_{12}(q) & -i\tilde{M}_{13}(q) & -i\tilde{M}_{14}(q) \\ i\tilde{M}_{12}(q) & \tilde{M}_{22}(q) & -i\tilde{M}_{23}(q) & -i\tilde{M}_{24}(q) \\ i\tilde{M}_{13}(q) & i\tilde{M}_{23}(q) & \tilde{M}_{33}(q) & -i\tilde{M}_{34}(q) \\ i\tilde{M}_{14}(q) & i\tilde{M}_{24}(q) & i\tilde{M}_{34}(q) & \tilde{M}_{44}(q) \end{bmatrix}, \tag{2.11}$$

where C_{ij} denotes the coefficients of the elastic tensor and

$$\begin{aligned}
\tilde{M}_{11}(q) = \tilde{M}_{33}(q) &= (1-r)\,\frac{\sinh(qh)\cosh(qh) - rqh}{f(q,h)},\\
-\tilde{M}_{12}(q) = \tilde{M}_{34}(q) &= \frac{1-r}{1+r}\,\frac{(1-r)\sinh^2(qh) - 2(rqh)^2}{f(q,h)},\\
\tilde{M}_{13}(q) &= (1-r)\,\frac{rqh\cosh(qh) - \sinh(qh)}{f(q,h)},\\
-\tilde{M}_{14}(q) = \tilde{M}_{23}(q) &= (1-r)\,\frac{rqh\sinh(qh)}{f(q,h)},\\
\tilde{M}_{22}(q) = \tilde{M}_{44}(q) &= (1-r)\,\frac{\sinh(qh)\cosh(qh) + rqh}{f(q,h)},\\
\tilde{M}_{24}(q) &= -(1-r)\,\frac{rqh\cosh(qh) + \sinh(qh)}{f(q,h)},
\end{aligned} \tag{2.12}$$

with

$$\begin{aligned}
f(q,h) &= \cosh^2(qh) - (rqh)^2 - 1,\\
r &= \frac{1-s}{1+s},
\end{aligned} \tag{2.13}$$

and $s = C_{44}/C_{11}$. In its simplest form, in the case of frictionless contact with a half-space and incompressible solid, tensor $\tilde{M}_{kl}(q)$ of Eq. 2.11 is reduced to a scalar $2(1-s)C_{44} \equiv E^*/2$, with $E^* = E/(1-\nu^2)$.

The remained unknown on the RHS of Eq. 2.4, the incremental iterative description of the interface interaction ${}^{(m+1)}\Delta\tilde{\mathbf{T}}_{\text{if}}(q)$, is thoroughly discussed in the following.

2.3. INTERFACE INTERACTION

At iteration $m+1$, the incremental interface interaction ${}^{(m+1)}\Delta\tilde{\mathbf{T}}_{\text{if}}(q)$ is first computed in real space:

$$\begin{aligned}
{}^{(m+1)}\Delta\mathbf{T}_{\text{if}} =& \mathbf{T}_{\text{if}}({}^{(m)}\Delta_{\text{n}},\, {}^{(m)}\Delta_{\text{t}}) - {}^{(t)}\mathbf{T}_{\text{if}}\\
&+ \left(\frac{\partial \mathbf{T}_{\text{if}}}{\partial \Delta_{\text{n}}}\right)_{{}^{(m)}\Delta_{\text{n}},\,{}^{(m)}\Delta_{\text{t}}} \times \delta\Delta_{\text{n}} + \left(\frac{\partial \mathbf{T}_{\text{if}}}{\partial \Delta_{\text{t}}}\right)_{{}^{(m)}\Delta_{\text{n}},\,{}^{(m)}\Delta_{\text{t}}} \times \delta\Delta_{\text{t}},
\end{aligned} \tag{2.14}$$

where ${}^{(m)}\Delta_t$ and ${}^{(m)}\Delta_n$ refer to the tangential and normal components of the gap function in the m-th iteration at time $t+\Delta t$. Here, $\delta\Delta_n$ and $\delta\Delta_t$ are defined as

$$\begin{aligned}\delta\Delta_n &:= {}^{(m)}\Delta_n - {}^{(m-1)}\Delta_n,\\ \delta\Delta_t &:= {}^{(m)}\Delta_t - {}^{(m-1)}\Delta_t.\end{aligned} \tag{2.15}$$

Subsequently, ${}^{(m+1)}\Delta\mathbf{T}_{if}$ is transformed to reciprocal space, ${}^{(m+1)}\Delta\widetilde{\mathbf{T}}_{if}(q)$.

On the RHS of Eq. 2.14, $\mathbf{T}_{if}$ is specified in terms of constitutive equations for traction components in normal and tangential directions, $T_{if,n}$ and $T_{if,t}$ respectively. In this work, $T_{if,n}$ and $T_{if,t}$ are obtained from coupled cohesive-zone relations.

COUPLED COHESIVE-ZONE MODEL

In the description of the interface as a cohesive surface, the interface tractions are determined as a function of the normal and tangential components of the gap function. Among the widening class of coupled CZMs, the Xu-Needleman model is one of the most frequently used [17]. In that model, the coupling between tangential and normal tractions is defined based on the parameter

$$c = \frac{\phi_t}{\phi_n}, \tag{2.16}$$

where ϕ_t and ϕ_n are the tangential and normal works of separation, respectively. van den Bosch *et al.* [18] showed that by employing the Xu-Needleman model, the required normal traction at complete shear failure reduces to zero if and only if $c = 1$. However, choosing $c = 1$ implies that $\phi_t = \phi_n$, while multiple experimental studies show that the normal and tangential works of separation are not necessarily equal to each other [19, 20]. Hence, an improved exponential law was proposed by van den Bosch *et al.* [18], the BSG model, which works very well for crack opening, less for indentation: the maximum tangential traction continues to decrease with increasing normal over-closure [21]. In fact, for large values of normal closure, a negative maximum tangential traction is obtained. In order to correct for this drawback, a modified form of the BSG model was proposed by McGarry *et al.* [21], the so-called NP1 model. This model eliminates the reduction in maximum tangential traction during mixed-mode closure and yet preserves all essential features of an improved exponential CZM.

In this work, following [21], the interface tractions are expressed as

$$T_{\mathrm{if,n}} = \frac{\phi_{\mathrm{n}}}{\delta_{\mathrm{n}}}\left(\frac{\Delta_{\mathrm{n}}}{\delta_{\mathrm{n}}}\right)\exp\left(-\frac{\Delta_{\mathrm{n}}}{\delta_{\mathrm{n}}}\right)\exp\left(-\frac{\Delta_{\mathrm{t}}^2}{\delta_{\mathrm{t}}^2}\right),$$
$$T_{\mathrm{if,t}} = 2\frac{\phi_{\mathrm{t}}}{\delta_{\mathrm{t}}}\left(\frac{\Delta_{\mathrm{t}}}{\delta_{\mathrm{t}}}\right)\exp\left(-\frac{\Delta_{\mathrm{n}}}{\delta_{\mathrm{n}}}\right)\exp\left(-\frac{\Delta_{\mathrm{t}}^2}{\delta_{\mathrm{t}}^2}\right), \tag{2.17}$$

where δ_{n} and δ_{t} are the characteristic lengths. The maximum values of $T_{\mathrm{if,n}}$ and $T_{\mathrm{if,t}}$ ($\sigma_{\max}$ and $\tau_{\max}$) are given as

$$\sigma_{\max} = \frac{1}{\exp(1)}\,\frac{\phi_{\mathrm{n}}}{\delta_{\mathrm{n}}}\,\exp\left(-\frac{\Delta_{\mathrm{t}}^2}{\delta_{\mathrm{t}}^2}\right),$$
$$\tau_{\max} = \frac{1}{\sqrt{0.5\exp(1)}}\,\frac{\phi_{\mathrm{t}}}{\delta_{\mathrm{t}}}\,\exp\left(-\frac{\Delta_{\mathrm{n}}}{\delta_{\mathrm{n}}}\right). \tag{2.18}$$

Coupled normal and tangential tractions versus normal and tangential gap values are graphically shown in Fig. 2.2.

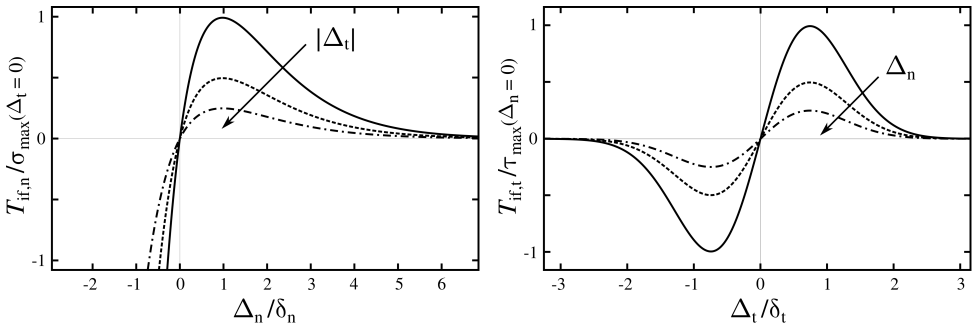

(a) Normal traction (b) Tangential traction

Figure 2.2: Graphical representation of coupled normal and tangential tractions versus normal and tangential gap values as given by Eq. 2.17.

In the case of non-adhesive contact, the normal interface interaction $T_{\mathrm{if,n}} = 0$ if $\Delta_{\mathrm{n}} \geq 0$ and hard-wall repulsion is assumed if $\Delta_{\mathrm{n}} < 0$. Besides, the tangential interface interaction $T_{\mathrm{if,t}} = 0$ on all surface nodes.

Note, the constitutive laws of Eq. 2.17 describe well the interface interaction between common materials [1]. If desired, it is possible to employ a different traction-separation law for modelling other systems, such as biological structures.

REFERENCES

[1] M. Khajeh Salehani, N. Irani, M. Müser, and L. Nicola, *Modelling coupled normal and tangential tractions in adhesive contacts,* Tribology International **124**, 93 (2018).

[2] V. L. Popov, I. A. Lyashenko, and A. E. Filippov, *Influence of tangential displacement on the adhesion strength of a contact between a parabolic profile and an elastic half-space,* Royal Society Open Science **4**, 161010 (2017).

[3] K.-S. Kim, R. McMeeking, and K. L. Johnson, *Adhesion, slip, cohesive zones and energy fluxes for elastic spheres in contact,* Journal of the Mechanics and Physics of Solids **46**, 243 (1998).

[4] I. A. Lyashenko, *Tangential displacement influence on the critical normal force of adhesive contact breakage in biological systems,* Facta Universitatis, Series: Mechanical Engineering **14**, 313 (2016).

[5] D. Maugis, *Adhesion of spheres: the JKR-DMT transition using a dugdale model,* Journal of Colloid and Interface Science **150**, 243 (1992).

[6] K. L. Johnson, *Adhesion and friction between a smooth elastic spherical asperity and a plane surface,* Proceedings of the Royal Society of London A: Mathematical, Physical and Engineering Sciences **453**, 163 (1997).

[7] R. A. Sauer and S. Li, *A contact mechanics model for quasi-continua,* International Journal for Numerical Methods in Engineering **71**, 931 (2007).

[8] S.-S. Cho and S. Park, *Finite element modeling of adhesive contact using molecular potential,* Tribology International **37**, 763 (2004).

[9] R. A. Sauer and S. Li, *An atomic interaction-based continuum model for adhesive contact mechanics,* Finite Elements in Analysis and Design **43**, 384 (2007).

[10] R. A. Sauer and P. Wriggers, *Formulation and analysis of a three-dimensional finite element implementation for adhesive contact at the nanoscale,* Computer Methods in Applied Mechanics and Engineering **198**, 3871 (2009).

[11] C. Campañá and M. H. Müser, *Practical Greens function approach to the simulation of elastic semi-infinite solids,* Physical Review B **74**, 075420 (2006).

[12] S. P. Venugopalan, L. Nicola, and M. H. Müser, *Green's function molecular dynamics: including finite heights, shear, and body fields,* Modelling and Simulation in Materials Science and Engineering **25**, 034001 (2017).

[13] N. Prodanov, W. B. Dapp, and M. H. Müser, *On the contact area and mean gap of rough, elastic contacts: Dimensional analysis, numerical corrections, and reference data,* Tribology Letters **53**, 433 (2014).

[14] D. Spence, *Self similar solutions to adhesive contact problems with incremental loading,* Proceedings of the Royal Society of London A: Mathematical, Physical and Engineering Sciences **305**, 55 (1968).

[15] L. Verlet, *Computer experiments on classical fluids. I. Thermodynamical properties of Lennard-Jones molecules,* Physical Review **159**, 98 (1967).

[16] S. P. Venugopalan, M. H. Müser, and L. Nicola, *Green's function molecular dynamics meets discrete dislocation plasticity,* Modelling and Simulation in Materials Science and Engineering **25**, 065018 (2017).

[17] X.-P. Xu and A. Needleman, *Void nucleation by inclusion debonding in a crystal matrix,* Modelling and Simulation in Materials Science and Engineering **1**, 111 (1993).

[18] M. Van den Bosch, P. Schreurs, and M. Geers, *An improved description of the exponential Xu and Needleman cohesive zone law for mixed-mode decohesion,* Engineering Fracture Mechanics **73**, 1220 (2006).

[19] W. Araki, K. Nemoto, T. Adachi, and A. Yamaji, *Fracture toughness for mixed mode I/II of epoxy resin,* Acta Materialia **53**, 869 (2005).

[20] M. Benzeggagh and M. Kenane, *Measurement of mixed-mode delamination fracture toughness of unidirectional glass/epoxy composites with mixed-mode bending apparatus,* Composites Science and Technology **56**, 439 (1996).

[21] J. P. McGarry, É. Ó. Máirtín, G. Parry, and G. E. Beltz, *Potential-based and non-potential-based cohesive zone formulations under mixed-mode separation and over-closure. part I: Theoretical analysis,* Journal of the Mechanics and Physics of Solids **63**, 336 (2014).

PART I

SINGLE–MODE LOADING

3

NON–ADHESIVE CONTACT

The relative contact area of rough surface contacts is known to increase linearly with reduced pressure. In its common definition, the reduced pressure contains the root-mean-square gradient (RMSG) of the entire surface. Although easy to measure, the RMSG of the entire surface may not coincide, at small loads, with the RMSG over the actual contact area. Considering the later definition for RMSG, first, a linear relation between contact area and reduced pressure is derived analytically for smooth asperity contacts and is used as a means of validation for the GFMD simulations. Then, the assumption of linearity for random rough non-adhesive contacts is assessed in line and surface contacts.

This chapter has been published in Tribology Letters **66**, 115 (2018) [1].

3.1. INTRODUCTION

IT is well established that for the elastic non-adhesive contact of random rough surfaces (2D), the equation

$$a_{\text{rel}} = \kappa\, p^* \tag{3.1}$$

provides a good description of the relation between the relative contact area a_{rel} and the reduced pressure p^* [2–9]. The relative contact area a_{rel} is defined as the ratio of the actual contact area a_{act} (the area over which the gap between the two solids is zero) to the nominal contact area a_{nom}. Besides, $p^* \equiv p/(\bar{g}\, E^*)$, where E^* is the contact modulus, p is the nominal contact pressure, and $\bar{g}$ is the root-mean-square gradient (RMSG) calculated over the nominal contact area. The linear relation in Eq. 3.1 holds true when the infinitesimal contact condition is assumed, i.e. p^* is small compared to 1. For surfaces with random roughness, several authors [3, 4, 8] have found a proportionality factor κ weakly dependent on the Hurst roughness exponent and slightly greater than 2.

Although the RMSG of the entire rough surface is easy to measure, it does not directly reflect the physics of the problem, given that it may not coincide with the RMSG over the actual contact area. It was recently shown by Müser [10], that Eq. 3.1 does not hold for 2D smooth asperity (Hertzian) contacts, unless one replaces $\bar{g}$ with the RMSG calculated over the *actual* contact area $\bar{g}_{\text{r}}$. In the case of random rough surface contacts, $\bar{g}$ and $\bar{g}_{\text{r}}$ are expected to be negligibly different [10], but it is unknown whether this is also the case for line contacts. Nonetheless, for line contacts, numerical data is often fitted to laws that enforce linearity by design, e.g. see the work by Scaraggi *et al.* [11].

The aims of this chapter are: (1) To demonstrated that also for 1D smooth asperity (cylindrical) contacts the linear relation of Eq. 3.1 holds if the RMSG is calculated over the actual contact area, instead of the nominal contact area. This is done by analytical calculations following the work by by Müser [10]. Thereafter, analytical results are used as a means of validation for the Green's function molecular dynamics (GFMD) simulations. (2) To asses the assumption of linearity for random rough contacts where the proportionality factor is computed using both definitions of RMSG in line and surface contacts. Moreover, a scaling factor between the values of proportionality factor for 1D and 2D contacts is found. In this analysis, besides random rough surfaces also single smooth asperities are considered.

The numerical analysis is performed by applying the GFMD technique to non-adhesive contacts between elastic solids. Throughout this chapter, the roughness is mapped on a rigid indenter and the substrate is a semi-infinite incompressible elastic solid with an initially flat surface.

3.2. SMOOTH ASPERITY CONTACT

Before modelling rough surfaces, it is shown in this section that the numerical results capture the proportionality factor κ_r for 1D and 2D smooth asperity contacts.

The analytical results for Hertzian (2D) contacts were provided by Müser [10]. In that study, the reduced pressure was defined as $p_r^* \equiv p/(\bar{g}_r E^*)$, with $\bar{g}_r$ being the RMSG calculated over the actual contact area, while p is load divided by an arbitrary but fixed reference area.

Here, it is demonstrated that also for cylindrical (1D) contacts the linear relation of Eq. 3.1 holds if the RMSG is calculated over the actual contact area, instead of the nominal contact area. This is done by analytical calculations, thereafter, analytical results are used as a means of validation for the GFMD simulations.

3.2.1. ANALYTICAL RESULTS

Consider an infinitely long and smooth cylinder that indents a semi-infinite incompressible elastic solid. The parabolic approximation of the height profile of the indenter is given by

$$h(\rho) = \frac{R}{2}\left(\frac{\rho}{R}\right)^2, \tag{3.2}$$

where ρ is the distance from the vertical axis of symmetry and R is the radius of the cylinder. First, It is assumed that the relation

$$a_{\mathrm{rel}} = \frac{\kappa_r p}{\bar{g}_r E^*}, \tag{3.3}$$

is valid for the current contact problem. By defining p as the load L averaged over the nominal contact area a_{nom}, this equation can be rewritten as

$$2c = \frac{\kappa_r L}{\bar{g}_r E^*}, \tag{3.4}$$

where c is the half-width of the actual contact area a_{act}. It follows from [12] that

$$L = \frac{\pi E^* c^2}{4R}. \tag{3.5}$$

Furthermore, the RMSG determined over the actual contact area $\bar{g}_r$, is obtained as

$$\bar{g}_r = \sqrt{\frac{2\int_0^c \left(\frac{\partial h}{\partial \rho}\right)^2 \mathrm{d}\rho}{2c}} = \frac{c}{R\sqrt{3}}. \tag{3.6}$$

Table 3.1: Cylindrical and Hertzian contact parameters

	a_{act}	L	$\bar{g}_{\text{r}}$	κ_{r}
1D (cylindrical)	$2c$	$\pi E^* c^2/(4R)$	$c/(R\sqrt{3})$	1.47
2D (Hertzian [10])	πc^2	$\sqrt{\pi}\Gamma(2)E^* c^3/(\Gamma(2.5)R)$	$c/(R\sqrt{2})$	1.66

Substituting the relations for L and $\bar{g}_{\text{r}}$ in Eq. 3.4 gives

$$\kappa_{\text{r}} = \frac{8}{\pi\sqrt{3}} \simeq 1.47. \tag{3.7}$$

Note that the obtained proportionality constant is smaller than that of the Hertzian contact (see Table 3.1 for a comparison), and the ratio is $\kappa_{\text{r}}^{1\text{D}}/\kappa_{\text{r}}^{2\text{D}} \simeq 0.88$.

3.2.2. COMPUTATIONAL RESULTS

In the GFMD simulations, the surface of the elastic solid is first discretized with a number of equi-spaced grid points, which interact with each other through an effective stiffness [13]. A minimum of $n = 2^{13}$ equi-spaced grid points in each direction are employed to discretize the surfaces. Here, the ratio of the width of the periodic unit cell $\mathscr{L}$ to indenter radius R is set as $\mathscr{L}/R = 4$. This guarantees that adjacent indenters do not interact within the selected pressure range.

For the numerical calculation of $\bar{g}_{\text{r}}$ the following procedure is adopted: If point i is in contact along the x- and/or the y-direction, the local mean-square gradient at point i is calculated as

$$g_i^2 = \frac{1}{2}\left[\left(\frac{h_i - h_{i+1}}{l}\right)^2 + \left(\frac{h_i - h_{i-1}}{l}\right)^2\right], \tag{3.8}$$

where h_i is the height profile of the indenter at point i and l is the spacing between the grid points. Subsequently, the value of $\bar{g}_{\text{r}}^2$ is obtained as

$$\bar{g}_{\text{r}}^2 = \frac{\sum_{i=1}^{n_{\text{act}}} g_i^2}{n_{\text{act}}}, \tag{3.9}$$

where n_{act} is the total number of actual contact points, i.e. the points where the gap between the two solids is zero.

Figure 3.1 presents the obtained proportionality factor κ_{r} as a function of the reduced pressure p_{r}^*. The agreement between the numerical and analytical results in Fig. 3.1 supports the validity of the numerical model. In the following, the same model is used to study random rough contacts.

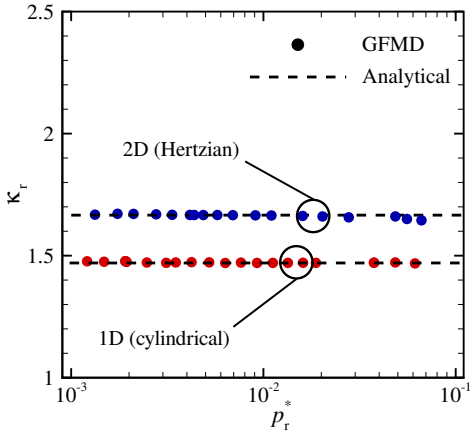

Figure 3.1: The computational and analytical results of the proportionality factor κ_r for smooth cylindrical and Hertzian contacts.

3.3. RANDOM ROUGH CONTACT

3.3.1. 1D PROBLEM

Here, it is assumed that the indenter has a self-affine roughness with a Gaussian height distribution. The roughness is generated by means of the spectral method described in [14]. The power spectrum density function $C(q)$ of the self-affine roughness [15] is given by

$$C(q) \equiv C(q_r) \times \begin{cases} 1 & \text{for } \lambda_r < \dfrac{2\pi}{q} \leq \mathscr{L}; \\ \left(\dfrac{q}{q_r}\right)^{-(1+2H)} & \text{for } \lambda_{s,H} < \dfrac{2\pi}{q} \leq \lambda_r; \\ 0 & \text{for } \lambda_s \leq \dfrac{2\pi}{q} \leq \lambda_{s,H}, \end{cases} \tag{3.10}$$

where the fractal dimension is $D_f = 2 - H$, and $C(q_r)$ is a scaling factor to obtain the desired RMSG $\bar{g}$ [16]. Here, λ_r is the roll-off wavelength, $\mathscr{L}$ the width of the periodic unit cell, $\lambda_{s,H}$ the roll-on wavelength, and λ_s the shortest wavelength. The value of $\bar{g}$ is taken to be constant and equal to 0.001. The roll-off wavelength is taken to be constant, $\lambda_r = 20$ μm. Besides, $\epsilon_t = \lambda_r/\mathscr{L}$ is set to 1/8 as according to [17] any $\epsilon_t \leqslant 1/4$ provides an acceptable probability density of heights for rough surfaces. The roll-on wavelength $\lambda_{s,H}$ is selected such that $\epsilon_f = \lambda_{s,H}/\lambda_r = 1/512$, similar to [11]. The continuum discretization $\epsilon_c = \lambda_s/\lambda_{s,H}$ is set equal to 1/64 [14]. This assures numerical convergence for all cases studied

here including low pressure values and all Hurst exponents, namely $H = 0.2$, 0.5, and 0.8, as discussed in [11].

In order to account for the random nature of the roughness, GFMD calculations are performed for 10 different randomly generated rough profiles for any given Hurst exponent. Thereafter, the statistical average is taken over the obtained results.

The numerical results of the relative contact area a_{rel} versus both reduced pressure $p^* \equiv p/(\bar{g}\,E^*)$ (in red) and $p_{\mathrm{r}}^* \equiv p/(\bar{g}_{\mathrm{r}}\,E^*)$ (in blue) are shown in Fig. 3.2a for the three selected Hurst exponents. Notice that the area-to-pressure relation

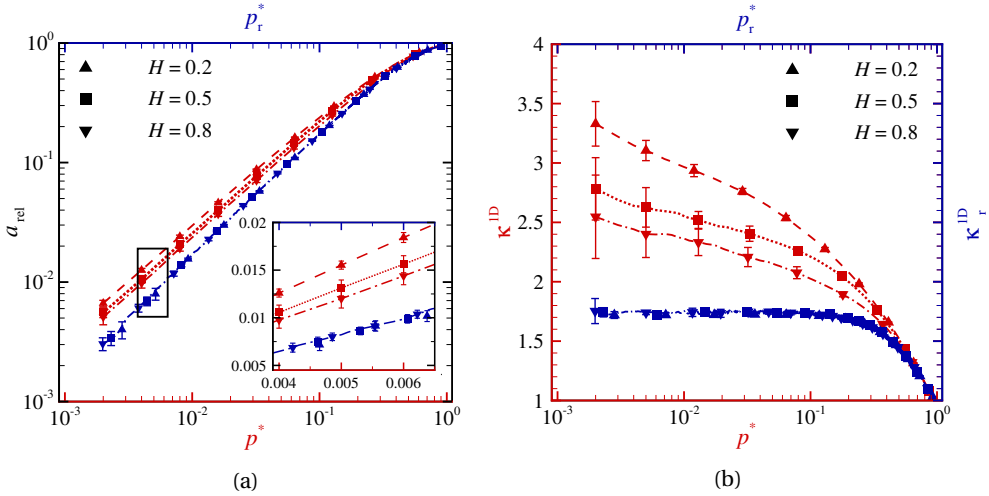

Figure 3.2: (a) The relative contact area a_{rel} versus both reduced pressure $p^* \equiv p/(\bar{g}\,E^*)$ (in red) and $p_{\mathrm{r}}^* \equiv p/(\bar{g}_{\mathrm{r}}\,E^*)$ (in blue) for line contacts with various H, obtained with GFMD simulations. (b) The data points from (a) are used to calculate $\kappa^{1\mathrm{D}}$ and $\kappa_{\mathrm{r}}^{1\mathrm{D}}$.

appears linear for both p^* and p_{r}^*; there is no dependence on the Hurst exponent for p_{r}^* and only negligible for p^*. However, if from the same data points the values of proportionality factors $\kappa^{1\mathrm{D}} \equiv a_{\mathrm{rel}}/p^*$ and $\kappa_{\mathrm{r}}^{1\mathrm{D}} \equiv a_{\mathrm{rel}}/p_{\mathrm{r}}^*$ are calculated, as presented in Fig. 3.2b, the following observations can be made:

- The proportionality factor $\kappa^{1\mathrm{D}}$ is not a constant and varies rather significantly (on average by ~ 25% in the pressure range spanning from $p^* = 10^{-1}$ to $p^* = 10^{-3}$).

- The proportionality factor $\kappa^{1\mathrm{D}}$ depends significantly on the Hurst exponent H.

- The proportionality factor $\kappa_r^{1D} \simeq 1.75$ is, on the contrary, constant and independent of H.

Therefore, it is concluded that similar to the case of smooth asperities, also for rough contacts the relation between relative contact area and reduced pressure is linear and independent of H, only if the RMSG is taken over the actual contact area. The value of the proportionality factor is $\kappa_r^{1D} \simeq 1.75$.

The results of κ in Fig. 3.2b indicate also that one should be careful when fitting data for line contacts with laws that result in a constant and single valued κ. In his theory of contact, Persson [2, 18] demonstrated that the relative contact area may be approximated by $a_{rel} = \text{erf}(\sqrt{2}p^*)$ for surface (2D) contacts. Later, Scaraggi *et al.* [11] proposed a correction to this equation so that it could be applied to line (1D) contacts:

$$a_{rel} = \text{erf}(\sqrt{2}\frac{p^*}{\Psi(p^*)}). \tag{3.11}$$

The correction function is defined as $\Psi(p^*) = b_1 + (1 - b_1)\,\text{erf}(b_2\, p^*)$, where b_1 and b_2 are fitting parameters.

By applying the approximation of Eq. 3.11 and calculate one fit to all our numerical results of relative contact area a_{rel} versus reduced pressure p^*, one obtains the proportionality factor κ_{fit}^{1D} presented with a dashed green line in Fig. 3.3. The results are in good agreement with the results of boundary elements simu-

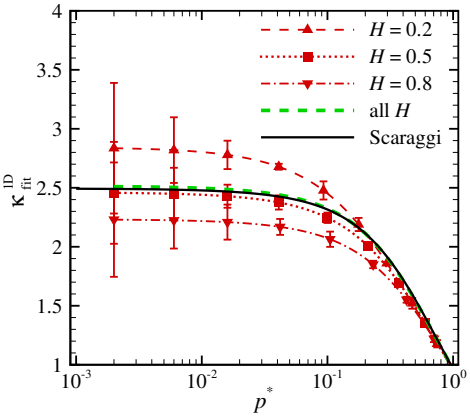

Figure 3.3: The proportionality factor κ_{fit}^{1D} versus reduced pressure p^* for profiles with Hurst exponent $H = 0.2$, 0.5, and 0.8 are shown with red lines. The fit obtained for all H (dashed green line) is also included along with the fit calculated for the results obtained by Scaraggi *et al.* [11] (solid black line). All curves are obtained using the approximation of Eq. 3.11.

lations performed by Scaraggi *et al.* [11] for profiles with various Hurst exponent

and RMSG (solid black line). However, if one calculates independent fits on the numerical results of a_{rel} versus p^* for each value of the Hurst exponent (see the red curves in Fig. 3.3), it may be found that $\kappa_{\text{fit}}^{\text{1D}}$ strongly depends on H, although for each Hurst exponent it is independent of reduced pressure when $p^* \lesssim 10^{-1}$. The latter is obviously expected, since linearity between relative contact area and reduced pressure is enforced by the fitting equation.

3.3.2. 2D PROBLEM

In this section, the proportionality factors for random rough surface contacts, computing RMSG over nominal and actual contact area, are calculated. Müser [10] stated that in this case, the difference between using $\bar{g}$ and $\bar{g}_{\text{r}}$ is not significant, i.e. $\kappa^{\text{2D}} \simeq \kappa_{\text{r}}^{\text{2D}}$. However, he did not explicitly quantify $\kappa_{\text{r}}^{\text{2D}}$. The aim of this section is, first, to verify that κ^{2D} and $\kappa_{\text{r}}^{\text{2D}}$ are in agreement and, second, to find the values of proportionality factor for surface contacts to be compared with the values obtained for line contacts in the previous section.

Here, the same roughness parameters as in Section 3.3.1 is considered except that $\epsilon_{\text{t}} = 1/4$ and $\epsilon_{\text{f}} = 1/64$ to keep the simulations computationally tractable. Besides, the fractal dimension $D_{\text{f}} = 3 - H$ and in the power spectrum density of Eq. 3.10 the power of q/q_{r} is $-2(1+H)$ [14].

Figure 3.4a shows the results of relative contact area a_{rel} versus both p^* (in

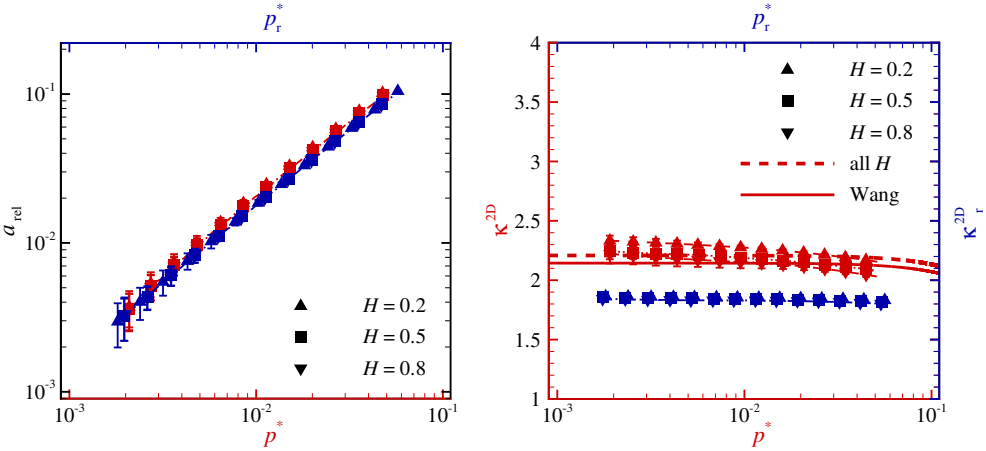

Figure 3.4: (a) GFMD results of the relative contact area a_{rel} versus p^* (red lines) and p_{r}^* (blue lines) for three values of Hurst exponent $H = 0.2$, 0.5, and 0.8. (b) The corresponding proportionality factors κ^{2D} and $\kappa_{\text{r}}^{\text{2D}}$ are plotted against p^* and p_{r}^*, respectively. Solid and dashed red lines are empirical fits to the results of Wang and Müser [19] and the current work, respectively.

red) and p_r^* (in blue). The data obtained for p^* and for p_r^* differs negligibly, i.e. much less than in the case of line contacts (compare with Fig. 3.2a). The corresponding proportionality factors κ^{2D} and κ_r^{2D} are shown in Fig. 3.4b. In this figure, the results are compared with those obtained by Wang and Müser [19]. In their work, they assumed that the results are independent of the Hurst exponent and obtained an empirical fit analogous to [2] on the numerical results of Prodanov *et al.* [8]. Here, the same empirical fit is applied to the numerical results (dashed red line in Fig. 3.4b). The difference between the obtained curve and Wang's is found to be negligible.

The results shown in Fig. 3.4b indicate that for surface contacts, the values of κ^{2D} and κ_r^{2D}, (even without using an empirical fit), are negligibly dependent on the Hurst exponent and the reduced pressure. Moreover, compared to the 1D case (see Fig. 3.3), κ^{2D} and κ_r^{2D} differ less, as $\kappa^{2D} \sim 2.20$ and $\kappa_r^{2D} \simeq 1.88$.

3.3.3. PROPORTIONALITY FACTOR: 1D VERSUS 2D

The results in terms of the ratio between the proportionality factors for line and surface contacts are shown in Fig. 3.5. Obviously, κ^{1D}/κ^{2D} is not a constant but depends on both Hurst exponent H and reduced pressure p^*, similar to κ^{1D}. The value of $\kappa_r^{1D}/\kappa_r^{2D}$ is constant and equal to 0.92.

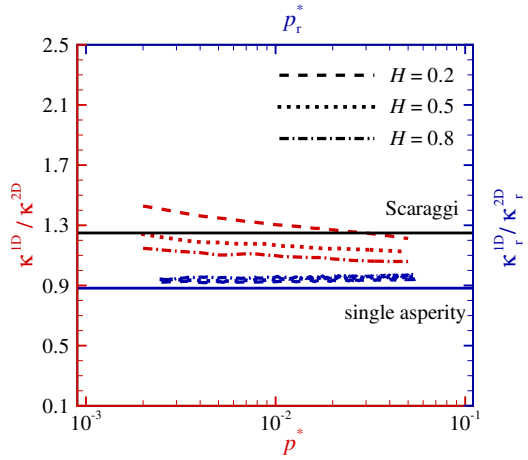

Figure 3.5: GFMD results for κ^{1D}/κ^{2D} and $\kappa_r^{1D}/\kappa_r^{2D}$ versus reduced pressure values p^* and p_r^*, respectively. Lines corresponding to the calculations of Scaraggi *et al.* [11] and the analytically obtained $\kappa_r^{1D}/\kappa_r^{2D}$ for single smooth asperity contacts (see Table 3.1) are also included in this figure.

The calculated value for the cylinder and Hertzian contacts is $\kappa_r^{1D}/\kappa_r^{2D} \simeq 0.88$ (see Table 3.1) and is also presented in Fig. 3.5. This value is remarkably close to the value obtained for $\kappa_r^{1D}/\kappa_r^{2D}$ for random rough contacts. Therefore, it is

concluded that the 1D-to-2D scaling factor, $\kappa_r^{1D}/\kappa_r^{2D} \sim 0.9$, can be used for both random rough and smooth contacts.

3.4. CONCLUSIONS

In this chapter, the numerical analysis is performed by applying the Green's function molecular dynamics (GFMD) technique to non-adhesive contacts between elastic solids. Throughout this chapter, the roughness is mapped on a rigid indenter and the substrate is a semi-infinite incompressible elastic solid with an initially flat surface.

First, it is demonstrated that for 1D smooth asperity (cylindrical) contacts, similar to 2D smooth asperity (Hertzian) cases, a linear relation can be obtained between contact area and reduced pressure only if the RMSG is calculated over the actual contact area ($\bar{g}_r$), instead of the nominal contact area ($\bar{g}$). This is done by analytical calculations, thereafter, analytical results are used as a means of validation for the GFMD simulations. Then, the assumption of linearity for random rough contacts is assessed where the proportionality factor is computed using both definitions of RMSG in line and surface contacts. This leads to the following conclusions:

- For rough line (1D) contacts, only when the RMSG is calculated over the *actual* contact area a linear relation exists between the relative contact area a_{rel} and the reduced pressure $p_r^* \equiv p/(\bar{g}_r E^*)$, such that the proportionality factor $\kappa_r^{1D} \simeq 1.75$ is independent of Hurst exponent and reduced pressure.
- For rough surface (2D) contacts, both the values of κ^{2D} and κ_r^{2D} are negligibly dependent on Hurst exponent and reduced pressure.
- Based on the obtained values for the proportionality factor κ_r in 1D and 2D contacts, a single 1D-to-2D scaling factor $\kappa_r^{1D}/\kappa_r^{2D} \sim 0.9$ is found for both rough and smooth asperity contacts.

It must be noted that measuring $\bar{g}$ experimentally is significantly easier than measuring $\bar{g}_r$ for which an in-situ measurement of the actual contact area [9, 20] would be required, while for computer simulations there is no significant difference in effort.

In the rest of this thesis, with extending the analysis to more complicated cases where considering interface interactions (adhesion and friction) and material compressibility, only line (1D) contact problems are addressed. The interest in studying 1D contacts, which is shared by various authors [11, 21–27], stems from the fact that 1D contacts are computationally less costly than 2D cases,

and therefore more suitable to study contact problems that go beyond simple non-adhesive cases. Moreover, rough surfaces in 1D contacts, contrary to their 2D counterparts, lack isotropy by definition. This is another reason for studying line contacts since in many practical applications rough surfaces are strongly anisotropic as a result of machining and surface treatment.

REFERENCES

[1] J. S. van Dokkum, M. Khajeh Salehani, N. Irani, and L. Nicola, *On the proportionality between area and load in line contacts,* Tribology Letters **66**, 115 (2018).

[2] B. N. Persson, *Theory of rubber friction and contact mechanics,* The Journal of Chemical Physics **115**, 3840 (2001).

[3] S. Hyun, L. Pei, J.-F. Molinari, and M. O. Robbins, *Finite-element analysis of contact between elastic self-affine surfaces,* Physical Review E **70**, 026117 (2004).

[4] C. Campañá and M. H. Müser, *Contact mechanics of real vs. randomly rough surfaces: A Green's function molecular dynamics study,* Europhysics Letters **77**, 38005 (2007).

[5] G. Carbone and F. Bottiglione, *Asperity contact theories: Do they predict linearity between contact area and load?* Journal of the Mechanics and Physics of Solids **56**, 2555 (2008).

[6] C. Yang and B. Persson, *Contact mechanics: contact area and interfacial separation from small contact to full contact,* Journal of Physics: Condensed Matter **20**, 215214 (2008).

[7] C. Putignano, L. Afferrante, G. Carbone, and G. Demelio, *The influence of the statistical properties of self-affine surfaces in elastic contacts: A numerical investigation,* Journal of the Mechanics and Physics of Solids **60**, 973 (2012).

[8] N. Prodanov, W. B. Dapp, and M. H. Müser, *On the contact area and mean gap of rough, elastic contacts: Dimensional analysis, numerical corrections, and reference data,* Tribology Letters **53**, 433 (2014).

[9] A. J. McGhee, A. A. Pitenis, A. I. Bennett, K. L. Harris, K. D. Schulze, J. M. Urueña, P. G. Ifju, T. E. Angelini, M. H. Müser, and W. G. Sawyer, *Contact*

and deformation of randomly rough surfaces with varying root-mean-square gradient, Tribology Letters **65**, 157 (2017).

[10] M. H. Müser, *On the linearity of contact area and reduced pressure,* Tribology Letters **65**, 129 (2017).

[11] M. Scaraggi, C. Putignano, and G. Carbone, *Elastic contact of rough surfaces: A simple criterion to make 2D isotropic roughness equivalent to 1D one,* Wear **297**, 811 (2013).

[12] K. L. Johnson, *Contact mechanics* (Cambridge University Press, Cambridge, 1985).

[13] C. Campañá and M. H. Müser, *Practical Greens function approach to the simulation of elastic semi-infinite solids,* Physical Review B **74**, 075420 (2006).

[14] M. H. Müser, W. B. Dapp, R. Bugnicourt, P. Sainsot, N. Lesaffre, T. A. Lubrecht, B. N. Persson, K. Harris, A. Bennett, K. Schulze, *et al.*, *Meeting the contact-mechanics challenge,* Tribology Letters **65**, 118 (2017).

[15] G. Carbone, M. Scaraggi, and U. Tartaglino, *Adhesive contact of rough surfaces: comparison between numerical calculations and analytical theories,* The European Physical Journal E **30**, 65 (2009).

[16] C. Campañá, M. H. Müser, and M. O. Robbins, *Elastic contact between self-affine surfaces: Comparison of numerical stress and contact correlation functions with analytic predictions,* Journal of Physics: Condensed Matter **20**, 354013 (2008).

[17] V. A. Yastrebov, G. Anciaux, and J.-F. Molinari, *From infinitesimal to full contact between rough surfaces: evolution of the contact area,* International Journal of Solids and Structures **52**, 83 (2015).

[18] G. Carbone, B. Lorenz, B. Persson, and A. Wohlers, *Contact mechanics and rubber friction for randomly rough surfaces with anisotropic statistical properties,* The European Physical Journal E **29**, 275 (2009).

[19] A. Wang and M. H. Müser, *Gauging Persson theory on adhesion,* Tribology Letters **65**, 103 (2017).

[20] B. Weber, T. Suhina, T. Junge, L. Pastewka, A. Brouwer, and D. Bonn, *Molecular probes reveal deviations from Amontons law in multi-asperity frictional contacts,* Nature Communications **9**, 888 (2018).

[21] W. Lai and H. Cheng, *Computer simulation of elastic rough contacts,* ASLE Transactions **28**, 172 (1985).

[22] K. Komvopoulos and D.-H. Choi, *Elastic finite element analysis of multi-asperity contacts,* Journal of tribology **114**, 823 (1992).

[23] Y. Ju and T. Farris, *Spectral analysis of two-dimensional contact problems,* Journal of Tribology **118**, 320 (1996).

[24] R. Sayles, *Basic principles of rough surface contact analysis using numerical methods,* Tribology International **29**, 639 (1996).

[25] A. Mihailidis, V. Bakolas, and N. Drivakos, *Subsurface stress field of a dry line contact,* Wear **249**, 546 (2001).

[26] J. Allwood, *Survey and performance assessment of solution methods for elastic rough contact problems,* Journal of Tribology **127**, 10 (2005).

[27] P. Sainsot and A. Lubrecht, *Efficient solution of the dry contact of rough surfaces: A comparison of fast fourier transform and multigrid methods,* Proceedings of the Institution of Mechanical Engineers, Part J: Journal of Engineering Tribology **225**, 441 (2011).

4

SMOOTH ASPERITY ADHESIVE CONTACT

The focus of this chapter is on the adhesive contact of a periodic array of smooth circular rigid asperities indenting into a flat deformable solid. The consequences of the interplay between adhesion and friction during single mode normal loading are investigated. Simulations are performed to evaluate the dependency of contact size, load-displacement curve and pull-off load on the interface properties. The results show that the contact size and the pull-off load increases with friction due to the adhesion and friction interplay. The effect of this interplay on both the contact size and the pull-off load is found to be strongest for highly adhesive contacts and materials with small Poisson's ratio.

This chapter has been published in Tribology International **124**, 93-101 (2018) [1].

4.1. INTRODUCTION

THE idea that adhesion and friction affect each other is generally attributed to Desaguliers (1734) [2]. However, it was Bowden and Tabor (1950) [3] who turned this idea into a principal part of their theory of friction. To gain a better understanding of the interplay between adhesion and friction, Savkoor and Briggs [4] applied tangential loading to a rubber hemisphere in an adhesive contact with a glass plate. From this experiment, they concluded that as a result of increasing the tangential force, the adhesive forces between the solids drop. Consequently, the contact size decreased and the surfaces peeled apart.

The aim of this chapter is to capture the consequences of the interplay between adhesion and friction during single mode normal loading. By employing the contact model described in Chapter 2, simulations are performed to evaluate the dependency of contact size, load-displacement curve and pull-off load on the interface properties.

Predicting the correct contact size is essential in various problems of practical importance, e.g. when evaluating the rate of adhesive wear [5], electrical and thermal conductance [6], and the leakage rate in sealed systems [7, 8]. Moreover, a proper estimation of the pull-off load, which is a widely accepted measure of adhesion [9], is necessary to predict delamination of coated layers [10, 11] or adhesion failure in microelectromechanical systems (MEMS) [12, 13].

While the formulation presented in Chapter 2 is applicable to linearly elastic solids with arbitrary material properties and a generic surface roughness, the focus of this chapter is on the adhesive contact of a periodic array of smooth circular rigid asperities indenting into a flat deformable solid. The effect of adhesion and friction interplay is examined for bodies with various Poisson's ratio and height, and for various contact spacing.

4.2. PROBLEM FORMULATION

The contact problem analysed in this chapter is sketched in Fig. 4.1. The surface of body 1 is flat and body 2 has a surface profile with circular protrusions repeating with periodicity w. Body 1 is taken to deform elastically with Young's modulus $E^{(1)} = 70$ GPa and various Poisson's ratios: $\nu^{(1)} = 0.1, 0.3$ and 0.45. Body 2 is taken to be rigid compared to body 1, with $E^{(2)} = 10^3 E^{(1)}$, and to indent it under plane strain conditions.

Unless otherwise specified, the height of body 1 is $h^{(1)} = 5$ μm and the width of the periodic unit cell is $w = 10$ μm. The effects of height and periodicity are explored by choosing $h^{(1)} = 20$ μm and $w = 2$ μm. The circular protrusions on the surface of body 2 have a radius of R = 25 μm.

The characteristic lengths of the CZM, δ_n and δ_t are set equal to 1 nm, since most clean surfaces adhere strongly in this order of separation [5]. Simulations are carried out for a wide range of normal work of separation, $\phi_n = 0.2-4.0$ N/m, typical range for solid interactions [14, 15], and tangential work of separation, $\phi_t/\phi_n = 0-1$ for all ϕ_n considered in this study.

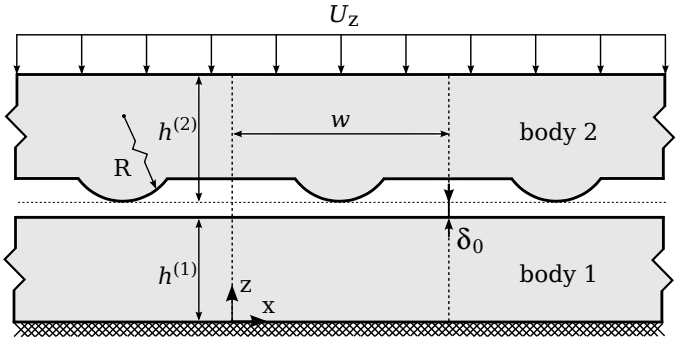

Figure 4.1: Sketch of the analysed two-dimensional indentation problem.

As sketched in Fig. 4.1 the origin of the coordinate system is fixed at the bottom corner of body 1. The bottom boundary of body 1 is fixed at $(x,z) = (x,0)$ and a uniform displacement U_z is applied on the top boundary of body 2. The displacement U_z is applied incrementally up to a final value of $20 \times \delta_n$ in 1000 increments. Also, the initial gap between the two solids is $\delta_0 = 10 \times \delta_n$. Note that for the applied displacement imposed, the size of the contact is much smaller than the width of the periodic unit cell. Therefore, the stress at the edge of the contact is not affected by the periodic boundary conditions [16].

The top and bottom boundaries of the periodic cell are discretized to 2^{11} equally spaced nodes. The employed parameters in the Verlet algorithm are $\eta \approx 1$ and $\delta t = 0.1$.

4.3. ADHESION AND FRICTION INTERPLAY

4.3.1. CONTACT SIZE

The reduced normal traction acting on the interface at final indentation depth ($U_z = 20 \times \delta_n$) is shown in Fig. 4.2a for two values of the tangential work of separation, $\phi_t = 0$ and $\phi_t = \phi_n$, which represent frictionless and strongly sticking contacts. Here, the contact size l_{rep} is defined as the size of the interface under repulsion. The figure shows that, for a given normal work of separation $\phi_n = 2.0$ N/m, an increase in tangential work of separation (ϕ_t) results in a higher repulsive force between the two solids. This is in line with the classical contact studies [17–19]

which predict that the load carrying capacity for sticking contacts is higher than for frictionless contacts.

Figure 4.2a also shows that, in the case of frictionless contact, $\phi_t = 0$, the adhesive force between the two solids is smaller when compared to the frictional case with $\phi_t = \phi_n$. The reason for this is that $|\Delta_t|$ increases with decreasing friction and this causes a reduction in the maximum normal strength, see Fig. 2.2a. In other words, the tangential displacement of two surfaces with respect to each other facilitates their normal decohesion, in line with [4, 20].

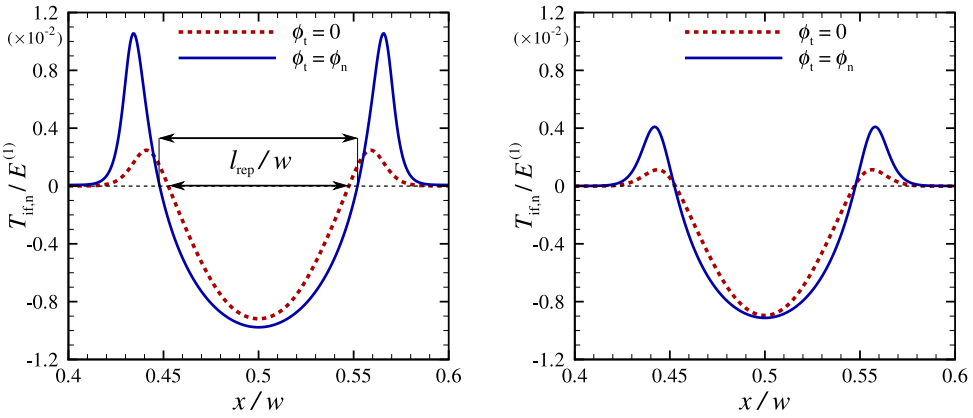

(a) $\phi_n = 2.0$ N/m (b) $\phi_n = 0.8$ N/m

Figure 4.2: Normal traction profiles for two values of the normal work of separation ϕ_n. In both figures, w/R = 0.4 and $\nu = 0.3$. Results are shown for $U_z = 20 \times \delta_n$.

In the frictionless case, smaller adhesion results in a smaller interface closure. Consequently, as can be seen from Fig. 4.2a, in the frictionless case, the contact size is ~ 10% smaller when compared to its frictional counterpart considered here. By comparing the results obtained for $\phi_n = 2.0$ N/m (Fig. 4.2a) and $\phi_n = 0.8$ N/m (Fig. 4.2b), it is observed that the effect of friction on contact size is more pronounced for interfaces with higher adhesion. Eventually, in the limit of non-adhesive contact conditions [17–19], contact size becomes independent of friction.

The dependency of contact size on friction is not observed for less compressible materials, i.e. materials with higher Poisson's ratio, as shown in Fig. 4.3a. This is due to the fact that for these materials, the tangential displacement of the surface is small and thus, there is less sliding at contact. Similarly, another case where contact size becomes independent of frictional conditions is when spacing between contacts is small, w/R $\to 0$, as shown in Fig. 4.3b. In this case, the

independency is due to interference of the tangential surface displacement of neighbouring contacts.

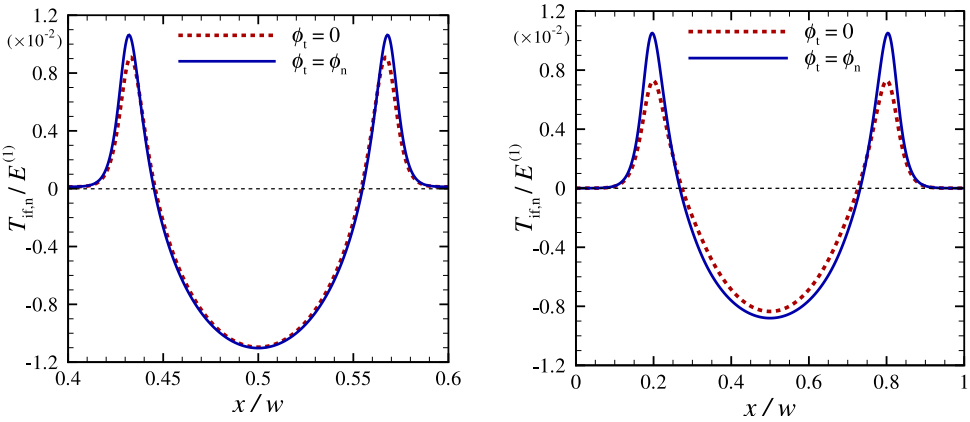

(a) $\nu \to 0.5$ (b) $w/\mathrm{R} \to 0$

Figure 4.3: Normal traction profiles for indenter with $w/\mathrm{R} = 0.4$ and substrate with $\nu = 0.45$ (a) and indenter with $w/\mathrm{R} = 0.08$ and substrate with $\nu = 0.3$ (b) in two different frictional conditions $\phi_\mathrm{t} = 0$ and $\phi_\mathrm{t} = \phi_\mathrm{n}$, where $\phi_\mathrm{n} = 2.0$ N/m in all cases. Results are shown for $U_\mathrm{z} = 20 \times \delta_\mathrm{n}$.

Figure 4.4a shows the variation of contact size with friction for different values of the normal work of separation. The results are plotted up to $\phi_\mathrm{t}/\phi_\mathrm{n} = 0.5$ where $\tau_{\max} \approx \sigma_{\max}$. Contact size is independent of friction when the normal work of separation is very small ($\phi_\mathrm{n} \leq 0.8$ N/m). Otherwise, a frictional contact has a contact area up to 15% larger than a frictionless contact. However, when the tangential work of separation reaches ~ 10% of the normal work of separation there is no further increase in the contact area. Variation of contact size with parameters other than friction is illustrated in Fig. 4.4b. For the sake of comparison, the blue curves in Figs. 4.4a and 4.4b are the same and represent the case: $\phi_\mathrm{n} = 2.0$ N/m, $\nu = 0.3$, $w/\mathrm{R} = 0.4$, and $h^{(1)}/\mathrm{R} = 0.2$. The following key features emerge from the figure:

- Increasing Poisson's ratio, where all other parameters are the same, results in larger contact size in indentation problems. This can be seen from Fig. 4.4b, by comparing the dashed red line for $\nu = 0.45$ with the solid blue line for $\nu = 0.3$.
- Decreasing spacing between contacts decreases the contact size, since the interference between indents facilitates deformation of the full surface. This is observed from Fig. 4.4b, by comparing the dotted green line for $w/\mathrm{R} = 0.08$ with the solid blue line for $w/\mathrm{R} = 0.4$.

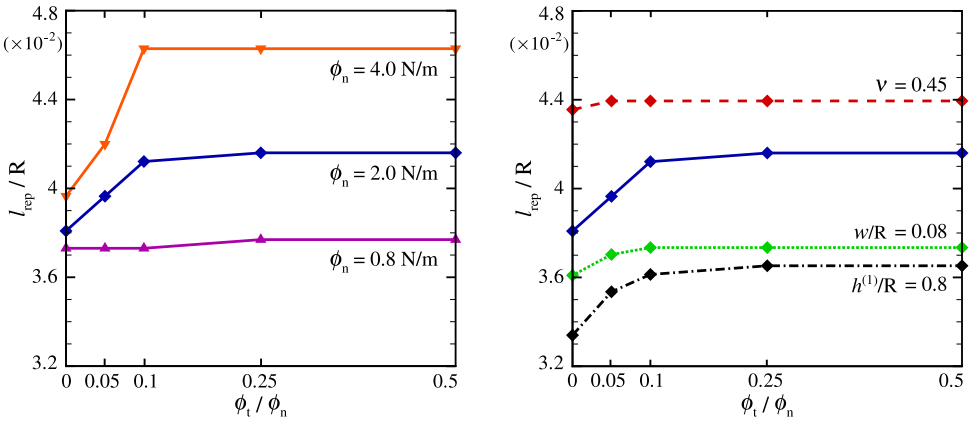

(a) $\nu = 0.3$, $w/\mathrm{R} = 0.4$, $h^{(1)}/\mathrm{R} = 0.2$ (b) $\phi_\mathrm{n} = 2.0$ N/m

Figure 4.4: Variation of the normalized value of the contact size, $l_\mathrm{rep}/\mathrm{R}$, with respect to the coupling parameter $c = \phi_\mathrm{t}/\phi_\mathrm{n}$. Results are shown for different values of the normal work of separation (a), Poisson's ratio, body height, and contact zone spacing (b) for $U_\mathrm{z} = 20 \times \delta_\mathrm{n}$. The solid blue lines are identical and used as a reference for comparison. Lines are a guide for the eye.

- Increasing height decreases contact size, yet it has negligible effect on the dependency of contact size on friction. This can be seen from Fig. 4.4b, by comparing the dash-dotted black line for $h^{(1)}/\mathrm{R} = 0.8$ with the solid blue line for $h^{(1)}/\mathrm{R} = 0.2$.

4.3.2. LOAD VERSUS DISPLACEMENT

In this section, the importance of considering the coupling between normal and tangential tractions is highlighted by comparing the load-displacement curves obtained using the coupled CZM of Eq. 2.17 with its uncoupled counterpart. The latter is obtained by removing the dependency on the tangential component from $T_\mathrm{if,n}$ in Eq. 2.17. Then, the normal interfacial traction in the uncoupled model is written as

$$T_\mathrm{if,n} = \frac{\phi_\mathrm{n}}{\delta_\mathrm{n}} \left(\frac{\Delta_\mathrm{n}}{\delta_\mathrm{n}}\right) \exp\left(-\frac{\Delta_\mathrm{n}}{\delta_\mathrm{n}}\right). \tag{4.1}$$

For both the coupled and uncoupled models, the contact is taken to be frictionless. The reason for this choice is that in a frictionless contact, $|\Delta_\mathrm{t}|$ is maximum, and therefore, the effect of coupling is strongest.

FRICTIONLESS CONTACT

Figure 4.5a compares the load-displacement curves obtained with coupled and uncoupled CZMs for two selected values of the normal work of separation. The

applied load L is calculated as

$$L = -\int_0^w T_{\text{if,n}}\, dx, \tag{4.2}$$

where the out-of-plane thickness of the bodies is considered to be unity, and chosen that an attractive force is negative. Then, inspired by the JKR and the DMT relations, the load is normalized as:

$$\overline{L} := \frac{L}{\pi\, \mathrm{R}\, \phi_0}, \tag{4.3}$$

where ϕ_0 is chosen to be 1 N/m and is only used for normalization. Moreover, the approach displacement is defined as $\delta := U_z - \delta_0$.

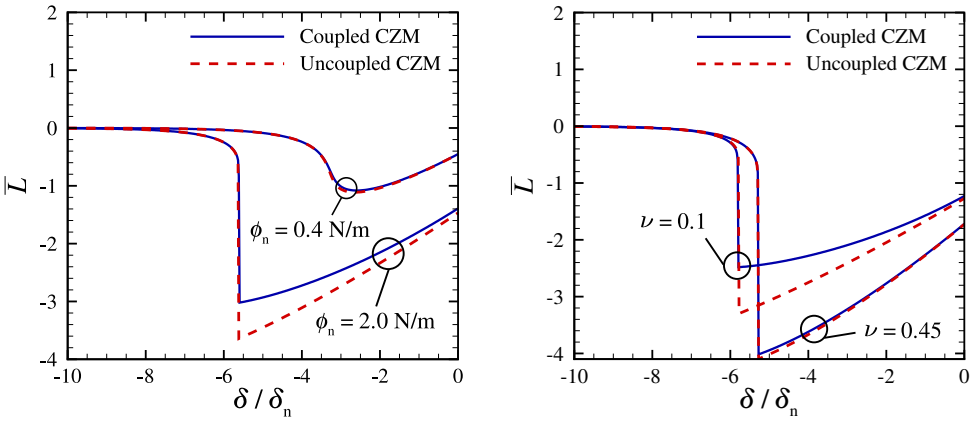

(a) $\nu = 0.3$ (b) $\phi_n = 2.0$ N/m

Figure 4.5: Normalized load versus normalized approach displacement for selected values of work of adhesion (a) and Poisson's ratio (b) by employing the coupled and uncoupled CZMs. For all cases the contact is taken to be frictionless.

As the two solids approach each other, the attraction force becomes stronger until it reaches a maximum value, the pull-off load. For the higher normal work of separation, $\phi_n = 2.0$ N/m, surfaces adhere abruptly, a behaviour often referred to as "jump-to-contact" [21]; while for lower normal work of separation, the jump-to-contact effect is not detected and the load increases gradually. Subsequently, as the gap closes further, some surface nodes get closer than the characteristic length and the attractive forces start to drop. Eventually, the gap closes with a number of surface nodes undergoing repulsion. The uncoupled CZM predicts a larger pull-off load than its coupled counterpart, especially for higher values of normal work of separation.

The effect of varying Poisson's ratio is shown in Fig. 4.5b. As to be expected, differences between coupled and uncoupled CZM results are insignificant for incompressible solids, where tangential displacements are negligible. It is however very pronounced for solids with $\nu = 0.1$, since $|\Delta_t|$ is large. Furthermore, a comparison between the coupled and uncoupled CZM predictions in Fig. 4.5b highlights that an uncoupled model tends to overestimate the pull-off load, especially for materials with smaller Poisson's ratio.

The results for both the coupled and uncoupled models demonstrate that beside the value of pull-off load, the position at which this maximum attractive load occurs, i.e. the pull-off distance, changes with the value of Poisson's ratio but is independent of the coupling. Figure 4.6 represents the deformed surface

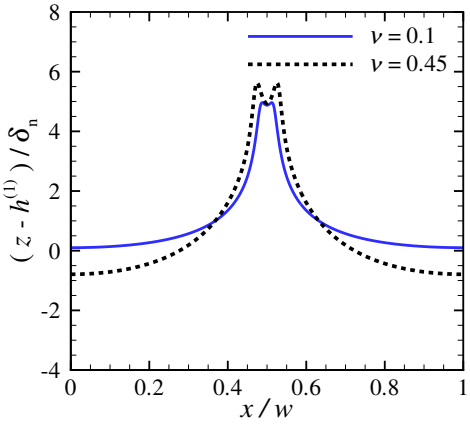

Figure 4.6: Deformed surface of body 1 at $\delta/\delta_n = -5$ for two values of Poisson's ratio. For $\nu = 0.45$, as the mid-part of the surface is pulled upwards, the rest of the surface tends to move downwards.

of body 1 at $\delta/\delta_n = -5$ for two selected values of Poisson's ratio. This figure illustrates that for materials with higher Poisson's ratio, because of incompressibility, as the mid-part of the surface is pulled upwards, the rest of the surface tends to move downwards and this subsequently, alters the pull-off distance.

FRICTIONAL CONTACT

The impact of friction on the evolution of load is presented in Fig. 4.7, by employing the coupled CZM and $\nu = 0.3$ with three selected values of tangential work of separation, ϕ_t. Figure 4.7 shows that, for the range of parameters used here, increasing friction leads to $\sim$ 16% increase in the pull-off load value, i.e. more frictional surfaces adhere stronger to each other. However, the pull-off distance is not affected noticeably by friction as shown in Fig. 4.7, since friction has a minor influence on the normal displacement of the surface.

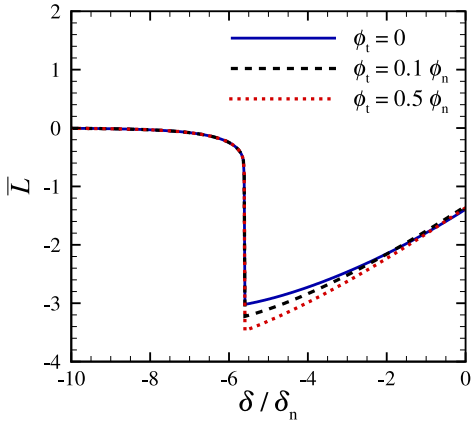

Figure 4.7: Normalized load versus displacement for three selected frictional conditions with $\nu = 0.3$ and $\phi_n = 2.0$ N/m, as obtained by the coupled CZM.

4.3.3. PULL-OFF LOAD

Finally, Fig. 4.8 illustrates the variation of the pull-off load with friction for two selected Poisson's ratios and various values of work of adhesion. Figure 4.8a shows that the evolution of the pull-off load versus work of adhesion for an almost in-

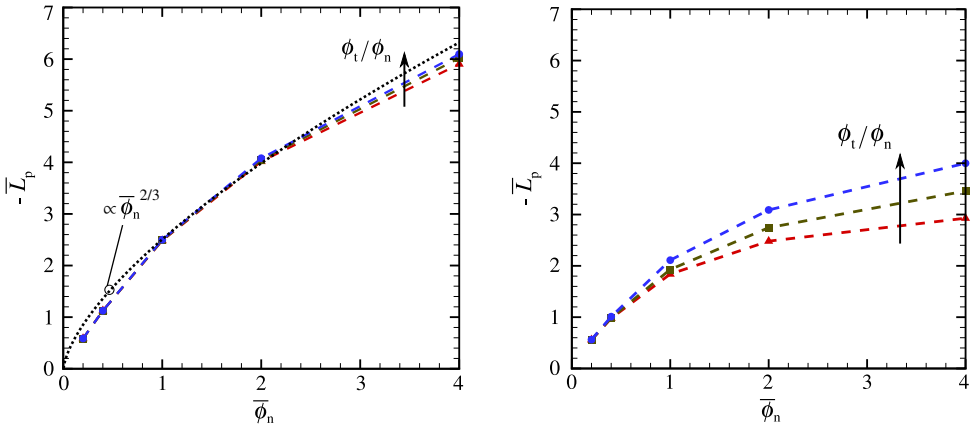

(a) $\nu = 0.45$ (b) $\nu = 0.1$

Figure 4.8: Normalized pull-off load versus normalized work of adhesion for Poisson's ratios equal to 0.45 (a) and 0.1 (b). Friction is increased by increasing ϕ_t/ϕ_n from 0 to 0.1 to 0.5. Dashed lines are a guide for the eye.

compressible solid is independent of friction and is proportional to $\overline{\phi}_n^{2/3}$, in line with the analytical solution for the adhesive contact of a cylindrical punch with

an incompressible elastic material [22, 23]. A quantitative agreement cannot be exact, given that the aforementioned analytical solution is derived under the assumptions that stresses at the edge of contact are infinite (JKR-type assumption), while the adhesive forces outside the contact area are neglected.

Comparison between Fig. 4.8b and Fig. 4.8a demonstrates that the pull-off load value decreases by decreasing Poisson's ratio and this decrease is stronger for higher values of adhesion and lower values of friction. Notice that each curve is plotted for a constant ϕ_t/ϕ_n ratio. For compressible solids there is an almost immediate deviation from the $\overline{\phi}_n^{2/3}$ analytical curve and different curves are necessary to represent the pull-off load values corresponding to different friction-to-adhesion ratios when $\overline{\phi}_n > 0.4$.

4.4. CONCLUSIONS

In this chapter, adhesive contact of a periodic array of smooth circular rigid asperities indenting into a flat deformable solid is studied. The aim of this study is to capture the consequences of the interplay between adhesion and friction during single mode normal loading. Simulations are performed to evaluate the dependency of contact size, load-displacement curve, and pull-off load on the interface properties. This dependency is examined for bodies with various Poisson's ratio and height, and for various contact spacing. This leads to the following conclusions:

- The relative tangential displacement between two surfaces is found to facilitate their normal decohesion.
- For a given normal work of separation, the contact size increases by increasing friction. The dependency of contact size on friction is observed for various heights of the deformable solid.
- Interplay between adhesion and friction results in a decrease of the pull-off load. The decrease is maximum for a frictionless surface, when sliding is maximum. Increasing friction increases the pull-off load.
- The effect of adhesion and friction interplay on both the contact size and the pull-off load is strongest for highly adhesive contacts and materials with small Poisson's ratio.
- The adhesion and friction interplay can be neglected in all cases when relative sliding of the surfaces is small, i.e. when one of these three conditions

hold: (1) friction is very large, (2) the material is incompressible, (3) contacts are closely spaced.

REFERENCES

[1] M. Khajeh Salehani, N. Irani, M. Müser, and L. Nicola, *Modelling coupled normal and tangential tractions in adhesive contacts,* Tribology International **124**, 93 (2018).

[2] K. L. Johnson, *Adhesion and friction between a smooth elastic spherical asperity and a plane surface,* Proceedings of the Royal Society of London A: Mathematical, Physical and Engineering Sciences **453**, 163 (1997).

[3] F. P. Bowden and D. Tabor, *The friction and lubrication of solids*, Vol. 1 (Oxford University Press, 1950).

[4] A. Savkoor and G. Briggs, *The effect of tangential force on the contact of elastic solids in adhesion,* Proceedings of the Royal Society of London A: Mathematical, Physical and Engineering Sciences **356**, 103 (1977).

[5] B. Bhushan, *Introduction to tribology* (John Wiley & Sons, 2013).

[6] M. Paggi and J. Barber, *Contact conductance of rough surfaces composed of modified RMD patches,* International Journal of Heat and Mass Transfer **54**, 4664 (2011).

[7] F. Pérez-Ràfols, R. Larsson, and A. Almqvist, *Modelling of leakage on metal-to-metal seals,* Tribology International **94**, 421 (2016).

[8] W. B. Dapp, A. Lücke, B. N. Persson, and M. H. Müser, *Self-affine elastic contacts: percolation and leakage,* Physical Review Letters **108**, 244301 (2012).

[9] R. Long and C.-Y. Hui, *The effect of preload on the pull-off force in indentation tests of microfibre arrays,* Proceedings of the Royal Society of London A: Mathematical, Physical and Engineering Sciences **465**, 961 (2009).

[10] M. Van den Bosch, P. Schreurs, and M. Geers, *An improved description of the exponential Xu and Needleman cohesive zone law for mixed-mode decohesion,* Engineering Fracture Mechanics **73**, 1220 (2006).

[11] P. Liu, Z. Gu, and X. Peng, *A nonlinear cohesive/friction coupled model for shear induced delamination of adhesive composite joint,* International Journal of Fracture **199**, 135 (2016).

[12] C. Mastrangelo, *Adhesion-related failure mechanisms in micromechanical devices,* Tribology Letters **3**, 223 (1997).

[13] Y.-P. Zhao, L. Wang, and T. Yu, *Mechanics of adhesion in MEMS–a review,* Journal of Adhesion Science and Technology **17**, 519 (2003).

[14] J. N. Israelachvili, *Intermolecular and surface forces* (Academic press, 2011).

[15] F. Aqra and A. Ayyad, *Surface energies of metals in both liquid and solid states,* Applied Surface Science **257**, 6372 (2011).

[16] V. L. Popov, R. Pohrt, and Q. Li, *Strength of adhesive contacts: Influence of contact geometry and material gradients,* Friction **5**, 308 (2017).

[17] O. Zhupanska and A. Ulitko, *Contact with friction of a rigid cylinder with an elastic half-space,* Journal of the Mechanics and Physics of Solids **53**, 975 (2005).

[18] V. Brizmer, Y. Kligerman, and I. Etsion, *The effect of contact conditions and material properties on the elasticity terminus of a spherical contact,* International Journal of Solids and Structures **43**, 5736 (2006).

[19] O. Zhupanska, *Axisymmetric contact with friction of a rigid sphere with an elastic half-space,* Proceedings of the Royal Society of London A: Mathematical, Physical and Engineering Sciences **465**, 2565 (2009).

[20] V. L. Popov, I. A. Lyashenko, and A. E. Filippov, *Influence of tangential displacement on the adhesion strength of a contact between a parabolic profile and an elastic half-space,* Royal Society Open Science **4**, 161010 (2017).

[21] B. Cappella and G. Dietler, *Force-distance curves by atomic force microscopy,* Surface Science Reports **34**, 15 (1999).

[22] M. Barquins, *Adherence and rolling kinetics of a rigid cylinder in contact with a natural rubber surface,* The Journal of Adhesion **26**, 1 (1988).

[23] M. K. Chaudhury, T. Weaver, C. Hui, and E. Kramer, *Adhesive contact of cylindrical lens and a flat sheet,* Journal of Applied Physics **80**, 30 (1996).

5

RANDOM ROUGH ADHESIVE CONTACT

Amontons' law of friction states that for any two materials contact area increases linearly with normal load. For non-adhesive contacts, it is well established that a linear relation exists between contact area and reduced pressure. In the case of adhesive contacts, however, there is not yet a general consensus on the linearity between contact area and normal load. In this chapter, the role of adhesion on the load-area relation for a wide range of interfacial properties is investigated. This is done by studying the contact response of an elastic solid indented by a self-affine rough rigid surface. For adhesive contacts the relation between the relative contact area and the reduced pressure is found to be non-linear. Non-linearity is more pronounced for rough profiles with a large Hurst exponent and/or small root-mean-square height. For rough profiles with a small Hurst exponent, non-linearity is significant only if the roughness is described using a large value for the small wavelength cut-off. Finally, it is found that the compressibility of the solid and frictional properties of the interface negligibly affect the load-area relation.

This chapter has been submitted for publication (2019) [1].

5.1. INTRODUCTION

THE understanding of friction relies on Amontons' law, which states that the friction force is directly proportional to the applied normal load. The common interpretation of this law is that the friction force increases linearly with contact area, which in turn increases linearly with the applied normal load. For non-adhesive elastic rough solids, state-of-the-art numerical simulations [2–10] have confirmed that there is indeed a linear relation between relative contact area and reduced pressure:

$$a_{\mathrm{rel}} = \kappa_{\mathrm{r}}\, p_{\mathrm{r}}^{*}. \tag{5.1}$$

The reduced pressure is defined as $p_{\mathrm{r}}^{*} := p/(\bar{g}_{\mathrm{r}}\, E^{*})$ where p is the load divided by an arbitrary but fixed reference area, E^{*} is the effective contact modulus, and $\bar{g}_{\mathrm{r}}$ is the root-mean-square gradient (RMSG) over the (real) contact area. Experiments performed on 3D printed rough surfaces seem to confirm the linear relationship [11, 12]. Very recently, Weber *et al.* [13] succeeded in the endeavour of visualizing *in situ* the increase in contact area during the indentation of a glass surface by means of two transparent rough materials: polystyrene (PS) and polymethyl-methacrylate (PMMA). Interestingly, they found that contact area does not increase linearly with the applied normal load. The reasons for the non-linearity in the experiment can be manyfold. In the literature two main possible causes for non-linearity have been identified: the plastic behaviour of materials [14], and the adhesive interaction between contacting surfaces. Interestingly, recent numerical studies on plasticity, although confined to metals, showed again linear area-to-load curves, albeit with a different slope than elasticity [15, 16].

Regarding adhesive contacts, there is not yet a general consensus on the linearity between contact area and normal load. Carbone *et al.* [17] studied contact between adhesive rough surfaces via numerical calculations, employing a boundary element method (BEM), and analytically, using an extended version of Persson's theory. They found that, even in the presence of adhesion, the contact area still linearly increases with the normal load. More recently, Rey *et al.* [18] obtained similar results using a fast Fourier transform (FFT) based BEM algorithm. However, the results obtained by Pastewka and Robbins [19], using a Green's function technique, and by Violano and Afferrante [20], employing Derjaguin-Muller-Toporov (DMT) methods, show a non-linear relation between contact area and normal load.

In order to shed more light on the observed differences in the linearity/non-linearity of the load-area relation, an extensive parameter study of interface and elastic properties is crucial. For example, Violano *et al.* [21], using an asymptotic

theory based on the DMT assumption, demonstrated that the small wavelengths of roughness are irrelevant. However, they only studied a rough profile with a large Hurst exponent $H = 0.8$. Furthermore, for the sake of simplicity, previous studies on the adhesive rough contacts were mainly focused on the frictionless interfaces and incompressible materials. The validity of these simplifications is needed to be examined.

Here, the adhesive elastic contact problem of a rough rigid solid indenting an initially flat deformable solid is studied. Simulations are performed using the Green's function molecular dynamics (GFMD) technique. The interactions between the surfaces are described through cohesive-zone (CZ) constitutive laws. The simulation results are presented for a wide range of interface and various elastic properties. New insights are provided into the role of roughness parameters (root-mean-square height, Hurst exponent, and small wavelengths), surface forces (adhesion and friction), and the compressibility of the solid on the relation between contact area and normal load.

5.2. PROBLEM FORMULATION

In this chapter, the indentation problem of a self-affine random rough rigid indenter into an initially flat deformable solid is studied. The interface interactions, adhesion and friction, are simultaneously active at the interface. The approach displacement is defined as $\delta := U_z - \delta_0$, where U_z is the applied normal displacement on the rigid indenter and δ_0 is the initial distance between the nearest point of the rough indenter and the solid (see Fig. 5.1). The main focus of

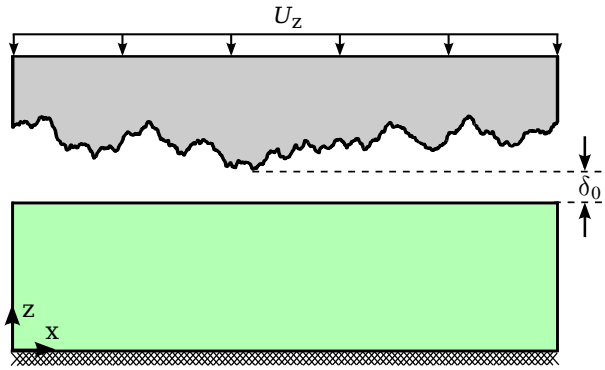

Figure 5.1: Sketch of the analysed contact problem.

this chapter is on the evolution of contact area versus normal load. The contact area is defined as the region of the interface where the magnitude of the inter-

action between surfaces (repulsive and/or attractive) is higher than a threshold value approaching zero.

For adhesive contacts, the cohesive-zone (CZ) constitutive laws are employed, as thoroughly discussed in Chapter 2, where are expressed as

$$T_{\mathrm{if,n}} = \frac{\phi_{\mathrm{n}}}{\delta_{\mathrm{n}}}\left(\frac{\Delta_{\mathrm{n}}}{\delta_{\mathrm{n}}}\right)\exp\left(-\frac{\Delta_{\mathrm{n}}}{\delta_{\mathrm{n}}}\right)\exp\left(-\frac{\Delta_{\mathrm{t}}^2}{\delta_{\mathrm{t}}^2}\right),$$
$$T_{\mathrm{if,t}} = 2\frac{\phi_{\mathrm{t}}}{\delta_{\mathrm{t}}}\left(\frac{\Delta_{\mathrm{t}}}{\delta_{\mathrm{t}}}\right)\exp\left(-\frac{\Delta_{\mathrm{n}}}{\delta_{\mathrm{n}}}\right)\exp\left(-\frac{\Delta_{\mathrm{t}}^2}{\delta_{\mathrm{t}}^2}\right). \tag{5.2}$$

Equation 5.2 can be employed for both compressible and incompressible solids. However, for a nearly incompressible solid (e.g., with Poisson's ratio $\nu = 0.45$) under pure normal loading, the relative tangential displacement of the surface nodes is negligible ($\Delta_{\mathrm{t}} \approx 0$), as discussed in [22]. Hence, Eq. 5.2 can be reduced to

$$T_{\mathrm{if,n}} = \frac{\phi_{\mathrm{n}}}{\delta_{\mathrm{n}}}\left(\frac{\Delta_{\mathrm{n}}}{\delta_{\mathrm{n}}}\right)\exp\left(-\frac{\Delta_{\mathrm{n}}}{\delta_{\mathrm{n}}}\right). \tag{5.3}$$

In the case of non-adhesive contacts, where $T_{\mathrm{if,t}} = 0$, and the normal interfacial interaction is controlled by a hard-wall potential.

5.2.1. CHOICE OF PARAMETERS

The deformable solid is elastic isotropic with elastic modulus 70 GPa and Poisson's ratio ranging from $\nu = 0.1$ to 0.45. Compared to the solid, the indenter is rigid, with $E_i = 1000\ E$. The dimensionless normal work of separation $\phi_{\mathrm{n}}^* = \phi_{\mathrm{n}}/(\delta_{\mathrm{n}}E)$ and $\phi_{\mathrm{t}}^* = \phi_{\mathrm{t}}/(\delta_{\mathrm{t}}E)$ is taken to range from 0.001 to 0.15, i.e. from weak adhesion as typical of metals, to strong adhesion as typical in bio-adhesives. Thus, within the elastic regime, findings in this chapter can be related to the experimental results for a wide class of materials, e.g., metals, elastomers and bio-adhesives. The tangential-to-normal work of separation is $c = \phi_{\mathrm{t}}^*/\phi_{\mathrm{n}}^*$. The effect of friction is studied by considering two values for the tangential-to-normal work of separation $c = \phi_{\mathrm{t}}^*/\phi_{\mathrm{n}}^*$: $c = 0$ for frictionless contacts and $c = 0.5$ for highly frictional contacts [22].

Simulations are carried out for various roughness parameters, namely Hurst exponent $H = 0.2,\ 0.5,\ 0.8$ and root-mean-square height $h_{\mathrm{rms}} = 10,\ 15,\ 30$ nm (for the full description of the roughness see Chapter 3). Convergence of the results is guaranteed by selecting $\epsilon_{\mathrm{t}} = \lambda_{\mathrm{r}}/\mathscr{L} = 8^{-1}$ and $\epsilon_{\mathrm{c}} = \lambda_{\mathrm{s}}/\lambda_{\mathrm{s,H}} = 32^{-1}$. The fractal discretization, which defines the number of wavelengths used to describe the rough profile, is chosen to be $\epsilon_{\mathrm{f}} = \lambda_{\mathrm{s,H}}/\lambda_{\mathrm{r}} = 512^{-1}$, and the role of the small

wavelengths on the load-area relation is assessed for $\epsilon_f = 128^{-1}$ and 64^{-1}. This is performed by keeping λ_r constant and choosing for the following values for $\lambda_{s,H} = 2.5, 10, 20$ nm.

To partly account for the random nature of the roughness, numerical calculations are performed for 10 different randomly generated rough profiles for any combination of H, h_{rms}, and ϵ_f. Thereafter, the average is taken over the obtained numerical results.

5.3. LOAD–AREA RELATION

5.3.1. ADHESIVE VERSUS NON–ADHESIVE CONTACTS

First, the results of relative contact area a_{rel} versus reduced pressure p_r^* for a solid with selected values of Poisson's ratio $\nu = 0.45,\ 0.1$ in a non-adhesive contact with a rigid rough profile with Hurst exponent $H = 0.2,\ 0.8$ and root-mean-square height $h_{rms} = 10,\ 30$ nm are shown in Fig. 5.2. This figure shows that the results

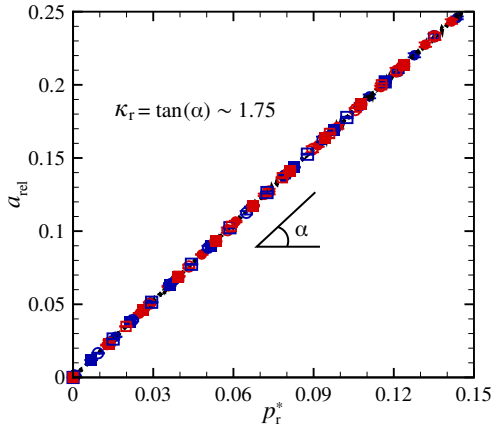

Figure 5.2: Non-adhesive contacts: relative contact area a_{rel} versus reduced pressure p_r^*. The results are shown for Hurst exponent $H = 0.2$ (squares) and $H = 0.8$ (circles), and Poisson's ratio $\nu = 0.45$ (red) and $\nu = 0.1$ (blue). Closed and open symbols are for root-mean-square height $h_{rms} = 10$ nm and $h_{rms} = 30$ nm, respectively. Note that error bars are smaller than the symbols.

are independent of both the compressibility of the solid and the roughness parameters considered. Furthermore, Fig. 5.2 also demonstrates that a_{rel} increases linearly with p_r^* in all cases. The proportionality factor is found to be ~ 1.75, in line with the results presented in Chapter 3. In the following, it is shown how adhesion affects the dependence of the relative contact area on reduced pressure.

Figure 5.3 presents the relative contact area a_{rel} versus reduced pressure p_r^* for a solid with Poisson's ratio $\nu = 0.45$ and an adhesive surface with various nor-

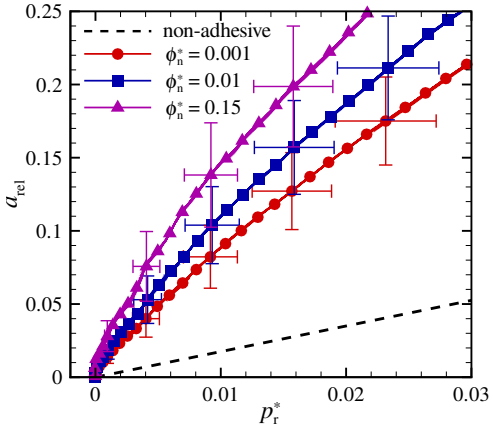

Figure 5.3: Adhesive contacts: relative contact area a_{rel} versus reduced pressure p_{r}^* for various normal works of separation ϕ_{n}^*. Dashed black line with the slope ~ 1.75 corresponds to the non-adhesive contact. The roughness parameters $H = 0.8$ and $h_{\text{rms}} = 10$ nm in all cases. For clarity only a selection of data points is shown.

5

mal works of separation ϕ_{n}^*. Note that such material is essentially incompressible [22] and hence, the interface interaction can be defined by Eq. 5.3. The result corresponding to the non-adhesive contact is also included in Fig. 5.3, shown by a dashed black line. Figure 5.3 shows that, as expected, for the same load, the contact area of adhesive contacts is larger than the non-adhesive case. More importantly, it is found that in adhesive contacts, the linearity between a_{rel} and p_{r}^* breaks down.

With the aim of improving the understanding of the observed differences between adhesive and non-adhesive contacts, the evolution of a_{rel}, p/E^*, and $\bar{g}_{\text{r}}$ versus approach displacement δ are individually investigated.

Figure 5.4a shows the evolution of the normalized pressure $p^* = p/E^*$ versus the approach displacement δ. Note that p is the sum of the normal tractions over the whole interface. The results in Fig. 5.4a show no difference between the calculated p^* in adhesive (various ϕ_{n}^*) and non-adhesive contacts. However, as illustrated in Fig. 5.4b, there is a significant difference between the RMSG calculated over the contact area for adhesive and non-adhesive cases. In this figure, $\bar{g}_{\text{r}}/\bar{g}$ is the RMSG over the contact area normalized by the RMSG over the nominal area, with the latter being the same in all cases. Figure 5.4b shows that in the case of non-adhesive contact, the RMSG over the contact area changes continuously. However, in adhesive contacts, $\bar{g}_{\text{r}}/\bar{g} \to 1$ very fast. It is worth mentioning that this trend is not specific of adhesive 1+1–D contacts, but also of non-adhesive 2+1–D contacts as shown in [10].

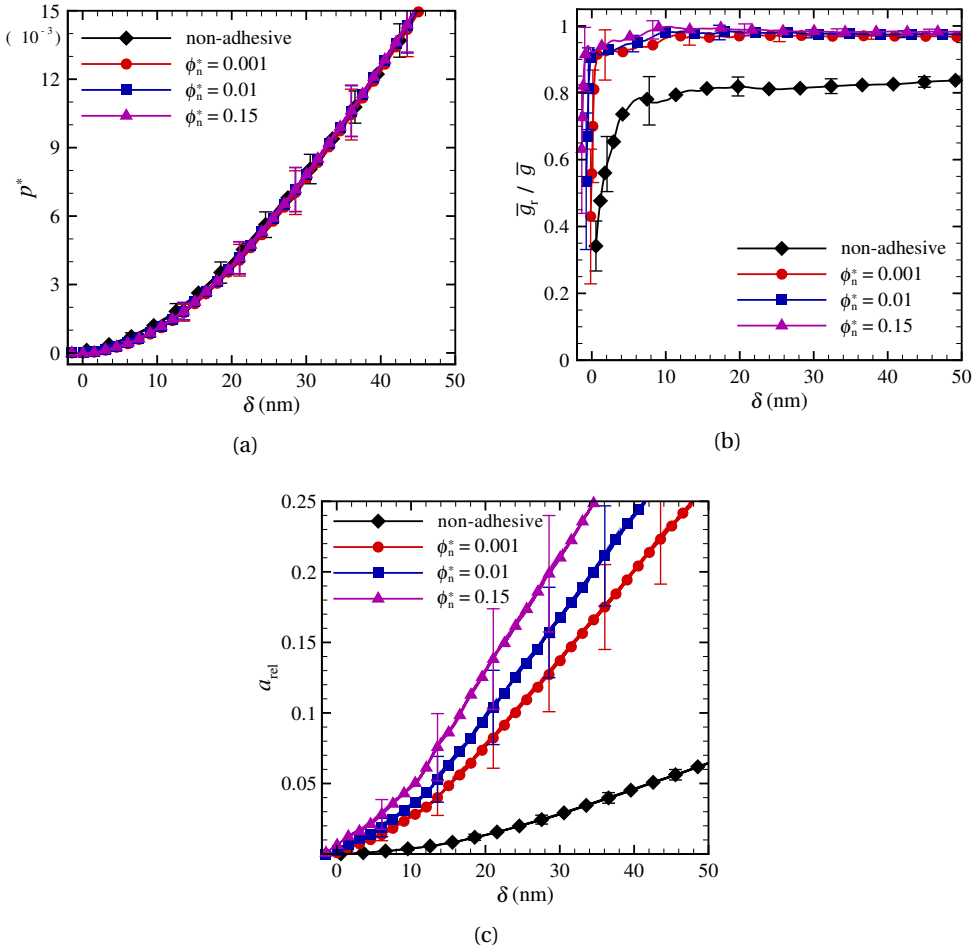

Figure 5.4: (a) Normalized pressure $p^* = p/E^*$, (b) Normalized root-mean-square gradient $\bar{g}_r/\bar{g}$, and (c) the relative contact area a_{rel} versus approach displacement δ. The results are shown for various normal works of separation ϕ_n^* (the same cases of Fig. 5.3). The roughness parameters $H = 0.8$ and $h_{rms} = 10$ nm.

As expected, Fig. 5.4c shows that also the relative contact area a_{rel} of an adhesive contact differs significantly from a non-adhesive contact. In the presence of adhesion, due to the attraction between surfaces, the deformable solid conforms better to the random rough rigid profile, particularly to the finer features of the roughness. This can be seen in Fig. 5.5 which shows a snapshot of the interface at $\delta = 20$ nm, for the cases shown in Fig. 5.4. With more adhesion, at the same

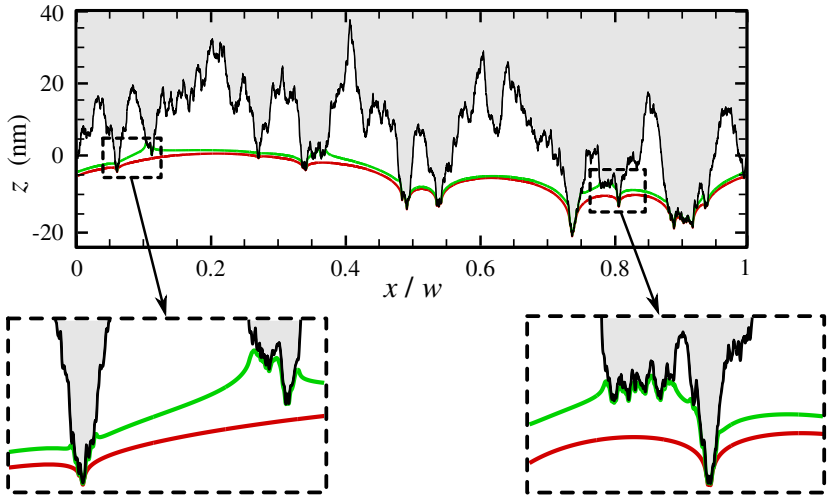

Figure 5.5: A snapshot of the interface at the approach displacement $\delta = 20$ nm. The results correspond to the cases shown in Fig. 5.4. The indenter is grey and the surface profiles of the adhesive ($\phi_{\text{n}}^* = 0.15$) and non-adhesive contacts are green and red, respectively.

indentation value a higher number of roughness peaks get into contact. Thus, it is observed that the error bars become larger with adhesion, e.g. see Fig. 5.4c.

As it has been shown in Chapter 3, for non-adhesive contacts by employing $p_{\text{r}}^* = p/(E^* \bar{g}_{\text{r}})$ instead of $p^* = p/E^*$ a linear relation is obtained between contact area and pressure. However, as presented in this section, in the presence of adhesion the linearity between a_{rel} and p_{r}^* breaks down. Hence, for the sake of simplicity, in the rest of this paper we only present our results as a function of the normalized pressure $p^* = p/E^*$.

5.3.2. ROLE OF ROUGHNESS PARAMETERS

For a solid with Poisson's ratio $\nu = 0.45$ and an adhesive surface with normal work of separation $\phi_{\text{n}}^* = 0.15$, Fig. 5.6 demonstrates that the evolution of the relative contact area a_{rel} versus the normalized pressure p^* is strongly dependent on the root-mean-square height h_{rms} and the Hurst exponent H. This figure shows that by increasing h_{rms} and/or decreasing H, a_{rel} significantly decreases for the same

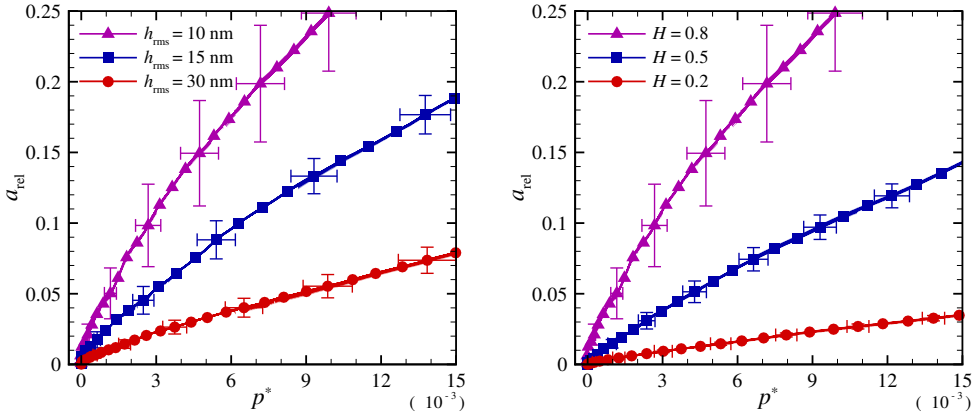

(a) $H = 0.8$ (b) $h_{rms} = 10$ nm

Figure 5.6: Relative contact area a_{rel} versus normalized pressure p^* for rough adhesive contact with various values of (a) root-mean-square height h_{rms} and (b) Hurst exponent H. The results are shown for the normal work of separation $\phi_n^* = 0.15$.

5

value of p^*. This is because for smaller H or larger h_{rms} the surface profile has more sharp protrusions, i.e. is more jagged. For such surfaces, (i) the gap at the interface and (ii) the gradient of the roughness become larger, thus a_{rel} decreases (as shown in Fig. 5.6). For small H and/or large h_{rms} the relation of a_{rel} with p^* approaches the linear relation of non-adhesive contacts.

In the following, it is investigated how the contact behaviour depends on the fine roughness features. Simulations are performed for rough profiles with fractal discretizations $\epsilon_f = 512^{-1}, 128^{-1}$, and 64^{-1}. The a_{rel} versus p^* are presented in Fig. 5.7a, for Hurst exponents $H = 0.8$ and 0.2. For $H = 0.8$, the $a_{rel} - p^*$ curve is independent of ϵ_f, in line with the work by Violano *et al.* [21]. On the contrary, for $H = 0.2$, the contact behaviour becomes strongly dependent on the smaller wavelengths: the contact area increases with increasing ϵ_f. This is because when the surface does not contain the smaller wavelengths the surface becomes smoother and hence, adheres better to the substrate, as can be seen from the snapshots in Fig. 5.7b.

5.3.3. ROLE OF COMPRESSIBILITY AND FRICTION

Finally, the role of compressibility and of the friction on the load-area relation is studied. Here, friction is included through the tangential work of separation ϕ_t^* different from zero. Unlike incompressible materials, for compressible materials the interface interaction is defined by the two cohesive laws in Eq. 5.2 instead of

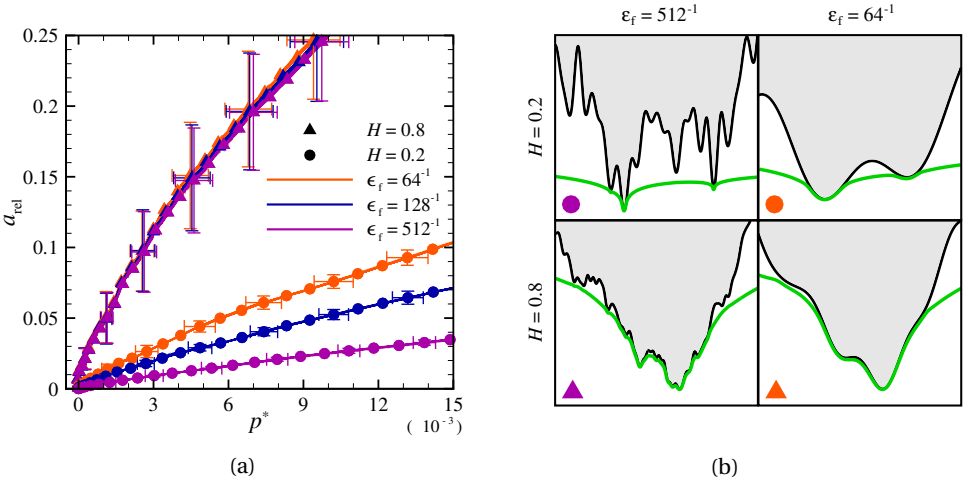

Figure 5.7: (a) Relative contact area a_{rel} versus normalized pressure p^* for various values of fractal discretization ϵ_f and Hurst exponent H. (b) Snapshots of a part of the interface for rough profiles with $\epsilon_f = 512^{-1}$, 64^{-1} and Hurst exponents $H = 0.8,\ 0.2$. In all cases, the root-mean-square height $h_{\text{rms}} = 10$ nm and the normal work of separation $\phi_n^* = 0.15$.

using the simple form of Eq. 5.3. Figure 5.8 shows the results for Poisson's ratio

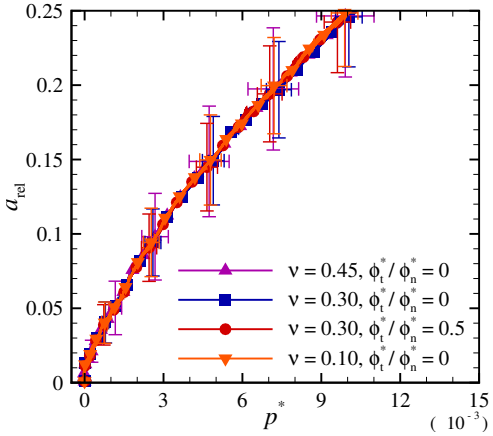

Figure 5.8: Relative contact area a_{rel} versus normalized pressure p^* for rough profile adhesive contacts. The results are shown for solids with various Poisson's ratios ν and interface friction properties. The normal work of separation $\phi_n^* = 0.15$, and the roughness parameters $H = 0.8$ and $h_{\text{rms}} = 10$ nm.

ν ranging from 0.1 to 0.45. This figure demonstrates that the $a_{\text{rel}} - p^*$ relation is negligibly affected by the compressibility of the solid and frictional properties of the interface.

This is in line with the findings in Chapter 4, where a solid was indented by an array of circular punches: when contacts are closely spaced the lateral displacement of the surface nodes is negligible, due to the interference of the displacement fields of the neighbouring punches.

5.4. CONCLUSIONS

The role of adhesion in the load-area relation in elastic contact problems is studied. Simulations are performed for the contact between a self-affine rough rigid surface and an initially flat deformable solid. The contact area of non-adhesive contacts linearly increases with reduced pressure, independently of Hurst exponent and root-mean-square height. In the presence of adhesion, the following key features are observed:

- The load-area relation is non-linear. Non-linearity is more pronounced for rough profiles with large Hurst exponent and/or small root-mean-square height.
- For small Hurst exponents the load-area relation depends on the small wavelengths cut-off used to described the roughness. In this case, non-linearity increases with increasing the small wavelength cut-off.
- Compressibility and friction can be neglected when investigating the load-area relation, since they affect it negligibly.

REFERENCES

[1] M. Khajeh Salehani, J. S. van Dokkum, N. Irani, and L. Nicola, *On the load–area relation in rough adhesive contacts,* Submitted for publication (2019).

[2] B. N. Persson, *Theory of rubber friction and contact mechanics,* The Journal of Chemical Physics **115**, 3840 (2001).

[3] S. Hyun, L. Pei, J.-F. Molinari, and M. O. Robbins, *Finite-element analysis of contact between elastic self-affine surfaces,* Physical Review E **70**, 026117 (2004).

[4] C. Campañá and M. H. Müser, *Contact mechanics of real vs. randomly rough surfaces: A Green's function molecular dynamics study,* Europhysics Letters **77**, 38005 (2007).

[5] G. Carbone and F. Bottiglione, *Asperity contact theories: Do they predict linearity between contact area and load?* Journal of the Mechanics and Physics of Solids **56**, 2555 (2008).

[6] C. Yang and B. Persson, *Contact mechanics: contact area and interfacial separation from small contact to full contact,* Journal of Physics: Condensed Matter **20**, 215214 (2008).

[7] C. Putignano, L. Afferrante, G. Carbone, and G. Demelio, *The influence of the statistical properties of self-affine surfaces in elastic contacts: A numerical investigation,* Journal of the Mechanics and Physics of Solids **60**, 973 (2012).

[8] N. Prodanov, W. B. Dapp, and M. H. Müser, *On the contact area and mean gap of rough, elastic contacts: Dimensional analysis, numerical corrections, and reference data,* Tribology Letters **53**, 433 (2014).

[9] A. J. McGhee, A. A. Pitenis, A. I. Bennett, K. L. Harris, K. D. Schulze, J. M. Urueña, P. G. Ifju, T. E. Angelini, M. H. Müser, and W. G. Sawyer, *Contact and deformation of randomly rough surfaces with varying root-mean-square gradient,* Tribology Letters **65**, 157 (2017).

[10] J. S. van Dokkum, M. Khajeh Salehani, N. Irani, and L. Nicola, *On the proportionality between area and load in line contacts,* Tribology Letters **66**, 115 (2018).

[11] L. Bartolome and W. Tato, *Experimental and numerical analysis of indentation on a thermoplastic polyurethane elastomer under cyclic loading,* in *European conference; 8th, Constitutive models for rubber* (CRC Press, 2013) pp. 649–656.

[12] B. Borovsky, J. Krim, S. Syed Asif, and K. Wahl, *Measuring nanomechanical properties of a dynamic contact using an indenter probe and quartz crystal microbalance,* Journal of Applied Physics **90**, 6391 (2001).

[13] B. Weber, T. Suhina, T. Junge, L. Pastewka, A. Brouwer, and D. Bonn, *Molecular probes reveal deviations from Amontons law in multi-asperity frictional contacts,* Nature Communications **9**, 888 (2018).

[14] F. S. Bąk, T. Trzepieciński, S. Bosiakov, and S. Rogosin, *Strain hardening effect on elastic-plastic contact of a rigid sphere against a deformable flat,* in *Advances in Mechanics: Theoretical, Computational and Interdisciplinary*

Issues: Proceedings of the 3rd Polish Congress of Mechanics (PCM) and 21st International Conference on Computer Methods in Mechanics (CMM), Gdansk, Poland, 8-11 September 2015, Vol. 549 (CRC Press, 2016) p. 77.

[15] L. Pei, S. Hyun, J. Molinari, and M. O. Robbins, *Finite element modeling of elasto-plastic contact between rough surfaces,* Journal of the Mechanics and Physics of Solids **53**, 2385 (2005).

[16] S. P. Venugopalan and L. Nicola, *Indentation of a plastically deforming metal crystal with a self-affine rigid surface: A dislocation dynamics study,* Acta Materialia **165**, 709 (2019).

[17] G. Carbone, M. Scaraggi, and U. Tartaglino, *Adhesive contact of rough surfaces: comparison between numerical calculations and analytical theories,* The European Physical Journal E **30**, 65 (2009).

[18] V. Rey, G. Anciaux, and J.-F. Molinari, *Normal adhesive contact on rough surfaces: efficient algorithm for FFT-based BEM resolution,* Computational Mechanics **60**, 69 (2017).

[19] L. Pastewka and M. O. Robbins, *Contact between rough surfaces and a criterion for macroscopic adhesion,* Proceedings of the National Academy of Sciences **111**, 3298 (2014).

[20] G. Violano and L. Afferrante, *On DMT methods to calculate adhesion in rough contacts,* Tribology International **130**, 36 (2019).

[21] G. Violano, L. Afferrante, A. Papangelo, and M. Ciavarella, *On stickiness of multiscale randomly rough surfaces,* arXiv:1810.10960 (2018).

[22] M. Khajeh Salehani, N. Irani, M. Müser, and L. Nicola, *Modelling coupled normal and tangential tractions in adhesive contacts,* Tribology International **124**, 93 (2018).

PART II

MIXED–MODE LOADING

6

FRICTIONAL SLIDING OF ADHESIVE CONTACT

Experiments show that when an adhesive contact is subjected to a tangential load the contact area reduces. What happens after the onset of sliding is more difficult to be assessed experimentally, especially under tensile loading. In this chapter, a complete picture of contact evolution of an adhesive circular smooth punch under mixed-mode loading, before and after sliding, is provided. First, the contact model introduced in Chapter 2 is extended to approach contact problems under mixed-mode loading. To this end, an interface model is developed where the interface interactions are described through sets of "springs", mimicking interatomic interactions. Next, simulations are performed to investigate frictional sliding of adhesive contact, under tension and compression. In line with the experimental observations, the reduction in the contact area during shear loading is found to be symmetric under tension and asymmetric under compression. After the onset of sliding and the occurrence of slip instability, the contact area abruptly increases (reattachment), under both tension and compression. For interfaces with high friction, the reattachment occurs only partially. However, a full reattachment is attainable when friction is low.

This chapter has been accepted for publication by Journal of the Mechanics and Physics of Solids (2019) [1].

6.1. INTRODUCTION

In the seminal work by Savkoor and Briggs (1977) [2] mixed normal and tangential loading was applied to a rubber hemisphere in adhesive contact with a glass plate. It was found that as a result of increasing the tangential load, the surfaces tend to peel apart and hence, the contact area decreases progressively. Later, Waters and Guduru [3] performed similar experiments for a wide range of normal loads (tensile and compressive) while continually recording images of the contact area evolution. These images demonstrated a symmetric contact area reduction under tensile loading and an asymmetric reduction under compressive loading, before the onset of sliding. Moreover, they captured a partial reattachment with the advent of slip instability at the interface under compressive loading. However, under tensile loading this reattachment was not observed. Recently, Sahli *et al.* [4] carried out experiments on an asperity sliding on a flat plate under compression and found that both smooth and rough asperities follow similar contact area–force equations during shear loading up to the onset of sliding.

The aim of this chapter is to develop a computational technique to study adhesive frictional contacts under mixed-mode (normal and tangential) loading that can reproduce the features observed in the above-mentioned experiments and predict the contact behaviour in conditions that are difficult to be achieved experimentally, i.e. after the onset of sliding. It is intended to provide a complete picture of the adhesive frictional problem for smooth contacts.

Adhesive contacts under mixed-mode loading have been extensively studied in [2, 3, 5–8] by using linear elastic fracture mechanics (LEFM) or the modified (mixed-mode) JKR adhesion theory, but these studies tackled exclusively non-slipping contacts. Adams [9] investigated adhesive contact of elastic cylinders under mixed-mode loading where both stick and slip regions can be present at the interface. Adams' analysis works well for compressive loading, but not for tensile loading: his formulation leads to negative contact sizes. Recently, Huang and Yan [10] introduced a model for sliding of adhesive contacts with the aim of analysing shearing problems under both compressive and tensile loading. With the same aim, Mergel *et al.* [11] developed a continuum contact model based on the finite element method (FEM). However, both works [10, 11] are limited to study the contact area evolution only up to the onset of sliding.

In this chapter, a complete picture of contact evolution under mixed-mode loading, before and after sliding, is provided. To this end, the two-solid contact model described in Chapter 2 is extended where the interactions between the surfaces are described through *sets* of "springs" that connect each surface node

with the nodes of the other surface. While the presented formulation is applicable to linearly elastic solids with a generic surface roughness obeying the small slope approximation, the focus of this chapter is on the contact shearing of a flat rigid substrate with a deformable solid. First, simulations are performed for flat-on-flat contact shearing to asses the capability of the model to capture the typical stick-slip motion during sliding [12, 13]. Then, the simulation results are presented for the adhesive frictional contact between a deformable circular protrusion and a flat rigid substrate.

6.2. METHODOLOGY

6.2.1. PROBLEM DEFINITION

A flat rigid substrate (body 1) is adjacent to an elastically deformable solid (body 2), having periodic circular protrusions with radius R, as schematically shown in Fig. 6.1. Periodicity is an intrinsic property of the Greens' function molecular dy-

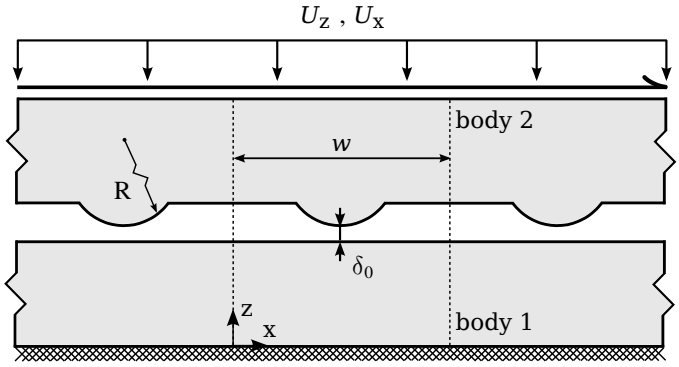

Figure 6.1: Sketch of the 1+1-dimensional contact problem.

namics model, which relies on the periodicity of Fourier transforms. The study in this chapter is focused on the behaviour of a single protrusion, therefore the width of the periodic unit cell w is taken to be large enough to guarantee that the asperity does not interact with its replicas within the range of applied loads.

The bottom boundary of body 1 is fixed. The minimum distance between the bodies is initially δ_0. A uniform normal displacement U_z^f is then applied at the top boundary of body 2, with the approach displacement defined as $\delta := U_z^f - \delta_0$. Next, a uniform tangential displacement U_x is exerted incrementally on the same boundary, while its vertical displacement is constrained.

6.2.2. INTERFACE INTERACTIONS

The interface interactions are modelled through sets of "springs" that connect the surface nodes, mimicking the interatomic interactions, as sketched in Fig. 6.2b. Red (or blue) springs represent the interactions between node i (or j) belonging

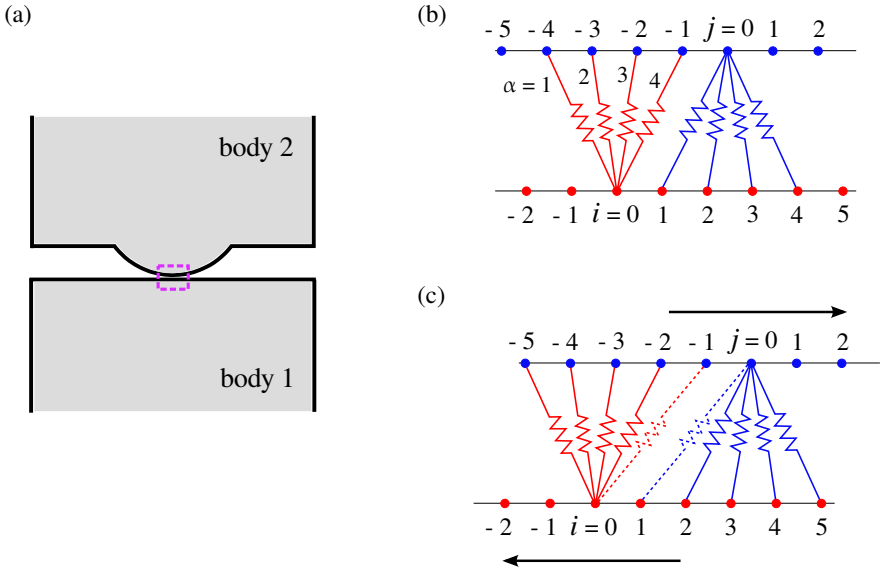

Figure 6.2: (a) Schematic representation of the bodies in contact. (b) The interface interactions are represented by springs for the region highlighted by a dashed rectangle. (c) The updated set of interaction springs, in a snapshot after sliding.

to the surface of a body and the nodes of the opposite surface. Figure 6.2c illustrates a snapshot of the same region shown in Fig. 6.2b after sliding, along with the updated set of interaction springs between the two surfaces. In principle, each node can be connected through springs to all other nodes of the surface of the counter-body. However, in practice, since the interactions with far away nodes is very weak, it is considered that each node reaches out with springs only to the nodes that fall within a "window". In Fig. 6.2c the dashed springs are those that fall outside of the window.

The interface model is implemented in the Green's function molecular dynamics (GFMD) technique described in [14] as follows. When the two solids under study are in mechanical equilibrium at time t, they exchange at the interface equal and opposite forces:

$$\mathbf{T}_{\text{if}}^{(1)} = -\mathbf{T}_{\text{if}}^{(2)} \qquad \forall\, t, \tag{6.1}$$

where $\mathbf{T}_{\text{if}}$ is the interface traction. The interface tractions acting on each node i

are computed as a sum over the m springs in the window:

$$\mathbf{T}_{\text{if}}(i) = \sum_{\alpha}^{m} \mathbf{T}_{\text{cz}}\left[\Delta_{\text{t}}(i,\alpha), \Delta_{\text{n}}(i,\alpha)\right], \tag{6.2}$$

where $\mathbf{T}_{\text{cz}}$ is the constitutive relation of each *individual* spring as a function of the tangential and normal gap values, i.e. the end-to-end distance of the springs:

$$\begin{aligned} \Delta_{\text{t}}(i,\alpha) &= x(j) - x(i), \\ \Delta_{\text{n}}(i,\alpha) &= z(j) - z(i), \end{aligned} \tag{6.3}$$

where j refers to each of the m nodes connected through springs to i.

In this work, $\mathbf{T}_{\text{cz}}$ is specified in terms of the cohesive-zone constitutive relations in normal and tangential directions, $T_{\text{cz,n}}$ and $T_{\text{cz,t}}$, which represent the adhesive and frictional forces per unit area, respectively. Similar to Chapter 2, following [15], the constitutive relations are expressed as

$$\begin{aligned} T_{\text{cz,n}} &= \frac{\phi_{\text{n}}}{\delta_{\text{n}}}\left(\frac{\Delta_{\text{n}}}{\delta_{\text{n}}}\right)\exp\left(-\frac{\Delta_{\text{n}}}{\delta_{\text{n}}}\right)\exp\left(-\frac{\Delta_{\text{t}}^2}{\delta_{\text{t}}^2}\right), \\ T_{\text{cz,t}} &= 2\frac{\phi_{\text{t}}}{\delta_{\text{t}}}\left(\frac{\Delta_{\text{t}}}{\delta_{\text{t}}}\right)\exp\left(-\frac{\Delta_{\text{n}}}{\delta_{\text{n}}}\right)\exp\left(-\frac{\Delta_{\text{t}}^2}{\delta_{\text{t}}^2}\right), \end{aligned} \tag{6.4}$$

where $(\phi_{\text{n}}, \phi_{\text{t}})$ and $(\delta_{\text{n}}, \delta_{\text{t}})$ are, respectively, the normal and tangential works of separation and characteristic lengths of each individual spring. Consequently, the maximum values of $T_{\text{cz,n}}$ and $T_{\text{cz,t}}$, i.e. the normal and tangential cohesive-zone strengths $\sigma_{\max}$ and $\tau_{\max}$, are given as

$$\begin{aligned} \sigma_{\max} &= \frac{1}{\exp(1)}\,\frac{\phi_{\text{n}}}{\delta_{\text{n}}}\,\exp\left(-\frac{\Delta_{\text{t}}^2}{\delta_{\text{t}}^2}\right), \\ \tau_{\max} &= \frac{1}{\sqrt{0.5\exp(1)}}\,\frac{\phi_{\text{t}}}{\delta_{\text{t}}}\,\exp\left(-\frac{\Delta_{\text{n}}}{\delta_{\text{n}}}\right). \end{aligned} \tag{6.5}$$

Cohesive-zone relations of Eq. 6.4 for normal and tangential tractions are graphically shown in Fig. 6.3 versus normal and tangential gap values, respectively. These relations describe well the interface interaction between common materials [14]. If desired, it is possible to employ a different “traction-separation" law for modelling other systems, such as biological structures.

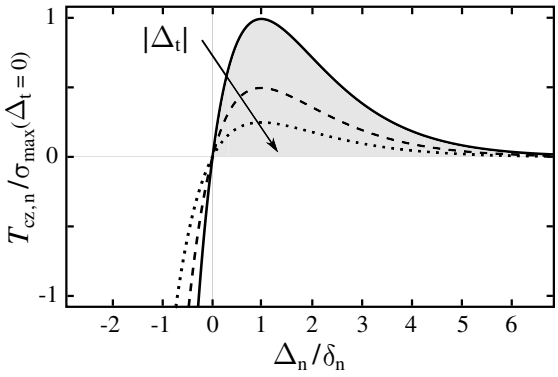

(a) normal traction

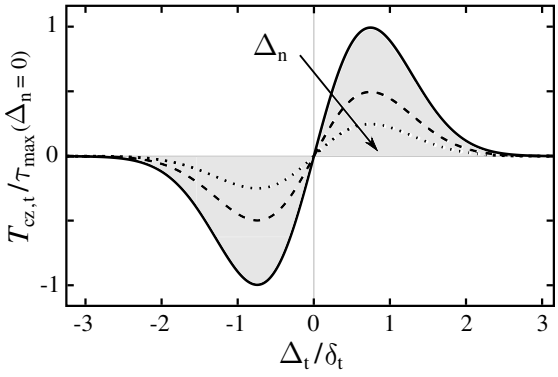

(b) tangential traction

Figure 6.3: Graphical representation of normal and tangential tractions versus normal and tangential gap values, as given by the cohesive-zone constitutive relations of Eq. 6.4.

6.2.3. CHOICE OF PARAMETERS

The circular protrusion on the surface of body 2 has a radius of $R/w = 2.5$, which is sufficiently large to obey the small slope approximation. The chosen material and interface properties are presented in terms of non-dimensional parameters $\overline{\square} = \square/\square^{\text{ref}}$, where the following "reference" parameters are used: $E^{\text{ref}} = 1$ GPa, $\phi_{\text{n}}^{\text{ref}} = \phi_{\text{t}}^{\text{ref}} = 1$ N/m, and $\delta_{\text{n}}^{\text{ref}} = \delta_{\text{t}}^{\text{ref}} = 1$ nm. The reference parameters are chosen to be unity and are only used for normalization. Unless otherwise specified, $\overline{\delta}_{\text{n}} = \overline{\delta}_{\text{t}} = 1$, $\overline{\phi}_{\text{n}} = 2$, the ratio of tangential-to-normal work of separation $\phi_{\text{t}}/\phi_{\text{n}} = 1$, and $\overline{E} = \overline{E}^{(2)} = 70$. Moreover, $E^{(1)} = 10^3 E^{(2)}$ (body 1 is assumed to be rigid) and $\nu = \nu^{(1)} = \nu^{(2)} = 0.45$. Here, it is opted for $\nu = 0.45$ since most of the experiments have been performed for almost incompressible materials.

The initial distance between the two solids is $\delta_0 = 10\,\delta_{\text{n}}$, which is large enough to have zero interface interactions at the beginning of the calculations (see Fig. 6.3a). Simulations are performed for a wide range of normal displacements $\overline{\delta} := \delta/\delta_0 = [-1, 1]$ in order to study both tensile and compressive loading. When considering flat-on-flat contact (no protrusion),it is taken $\overline{\delta} = 0$, so that $\Delta_{\text{n}} = 0$ all over the interface, providing the opportunity to assess the model in pure-shear mode (see Eq. 6.4).

The applied tangential displacement U_{x} is normalized on the width of the unit cell $\overline{U}_{\text{x}} = U_{\text{x}}/w$. The tangential and normal contact forces are, respectively, calculated as

$$\begin{aligned} F &= \int_0^w T_{\text{if,t}}^{(1)}\, dx = -\int_0^w T_{\text{if,t}}^{(2)}\, dx, \\ L &= -\int_0^w T_{\text{if,n}}^{(1)}\, dx = \int_0^w T_{\text{if,n}}^{(2)}\, dx, \end{aligned} \tag{6.6}$$

where it is considered that the out-of-plane thickness of the solids is unity, and chosen that an attractive normal force is negative. These contact forces are normalized as $\overline{F} = (F/w)/E$ and $\overline{L} = (L/w)/E$. The contact area A is defined as the size of the interface under repulsion and is normalized as $\bar{A} = A/w$.

The numerical convergence is guaranteed by employing an incremental displacement $\Delta U_{\text{z}} = \delta_{\text{n}}/10$ and $\Delta U_{\text{x}} = \delta_{\text{t}}/10$. To make the simulations computationally more efficient, the interaction between two opposite nodes is considered only if they fall within an interaction "window". The size of this window is independent of the surface discretization and is determined by the range of the cohesive-zone interactions. A converged solution is achieved by setting the window-size to $10\,\delta_{\text{n}}$ in normal and $5\,\delta_{\text{t}}$ in tangential directions.

6.3. FLAT-ON-FLAT CONTACT

Simulations are first performed for flat-on-flat contact under simple shearing to asses the capability of the model to predict the stick-slip motion observed experimentally [12] and via atomistic simulations [13], but smoothed out in most of the macroscopic models, e.g. see [6, 11]. Besides, the transition from stick-slip motion to continuous sliding is captured, where the dissipated energy becomes negligible [16] and hence, an ultra low friction regime can be achieved.

Results for various values of elastic modulus $\overline{E}$ and tangential work of separation $\overline{\phi}_t$ in Fig. 6.4a indeed show the typical sawtooth behaviour [12, 13] of the tangential contact force $\overline{F}$ versus the applied tangential displacement $\overline{U}_x$. In

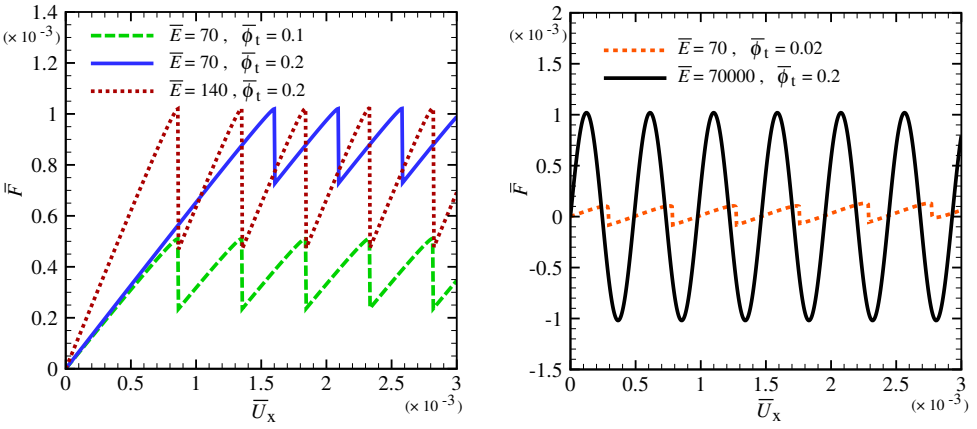

(a) stick-slip motion

(b) continuous sliding

Figure 6.4: Tangential contact force $\overline{F}$ versus applied tangential displacement $\overline{U}_x$ for various values of elastic modulus $\overline{E}$ and tangential work of separation $\overline{\phi}_t$. A transition is observed from stick-slip motion (a) to continuous sliding (b) by increasing $\overline{E}$ or decreasing $\overline{\phi}_t$. In all cases, the elastic modulus $\overline{E} = 70$ is used in normalizing the tangential contact force.

all cases, in the initial sticking stage, the force increases linearly with applied tangential displacement, with a slope controlled by $\overline{E}$. The force then drops abruptly as the two solids slip over each other. For stiffer materials, the stored elastic energy is larger and is released by a larger drop in force at each slip instability. This can be seen by comparing the blue solid line for $\overline{E} = 70$ and the dotted red line for $\overline{E} = 140$ in Fig. 6.4a. Moreover, as expected, as the interface interactions become weaker (by decreasing the tangential work of separation $\overline{\phi}_t$) the onset of sliding occurs at a lower tangential contact force $\overline{F}$. This can be observed by comparing the solid blue line for $\overline{\phi}_t = 0.2$ and the dashed green line for $\overline{\phi}_t = 0.1$ in Fig. 6.4a.

As shown in Fig. 6.4b, a transition from stick-slip motion to continuous slid-

ing is observed either when $\overline{\phi}_t$ is decreased or when $\overline{E}$ is increased . In the continuous sliding regime, the tangential contact force oscillates around zero with no initial sticking stage. In this case, the dissipated energy during sliding becomes negligible and hence, an ultra low friction regime is achieved. This is in line with the predictions of the Prandtl–Tomlinson model for cases in which the contact potential corrugation is low enough (low $\overline{\phi}_t$ in this work) and/or the stiffness of the system is high enough (high $\overline{E}$ in this work) [16].

Here, the friction force $\langle \overline{F} \rangle$ is calculated as the average of the maximum and the minimum tangential contact force during sliding [16], $\overline{F}_s$ and $\overline{F}_k$:

$$\langle \overline{F} \rangle = \frac{\overline{F}_s + \overline{F}_k}{2}. \tag{6.7}$$

Figure 6.5 shows a monotonic reduction in $\langle \overline{F} \rangle$ with increasing E and/or decreasing τ_{max}. It comes as no surprise that friction depends on the contact conditions (various τ_{max}), however, the fact that friction depends on the elastic modulus E needs further explanations. For materials with higher E, the larger drop in the tangential contact force leads to a decrease in the mean value of $\langle \overline{F} \rangle$. Eventu-

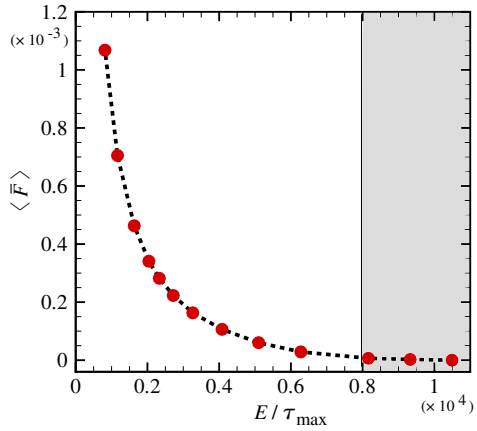

Figure 6.5: Friction reduces by increasing E/τ_{max}. Shaded area indicates the ultra low friction regime. The dashed line is a guide for the eye.

ally, by further increasing E, the friction force becomes negligible and an ultra low friction regime is achieved (see Fig. 6.5). On the contrary, the friction force increases as the solid becomes more compliant (lower E), in line with [17].

6.4. CIRCULAR PROBE ON FLAT SURFACE

Here, simulations are performed for adhesive frictional contact of a deformable solid with circular protrusion on a flat rigid substrate under mixed-mode loading. In this case, beside the tangential contact force, the evolution of the normal contact force and the change in the contact area are investigated.

The tangential contact force $\overline{F}$ versus applied tangential displacement $\overline{U}_{\mathrm{x}}$, for normal displacement $\overline{\delta} = 0$ and an interface with $\overline{\phi}_{\mathrm{n}} = \overline{\phi}_{\mathrm{t}} = 2$, is shown with the solid blue line in Fig. 6.6. In this figure, similar to the case of flat-on-flat

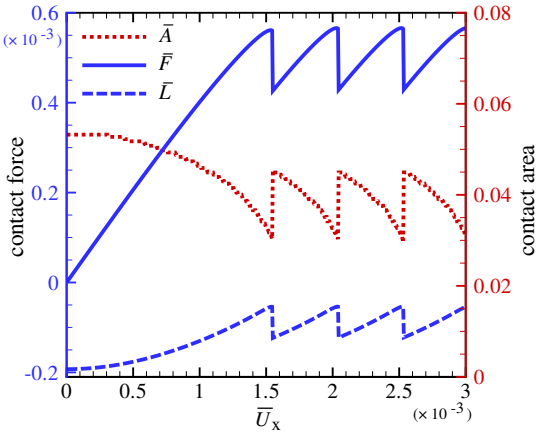

Figure 6.6: Evolution of the tangential $\overline{F}$ and the normal $\overline{L}$ contact forces, and the contact area $\bar{A}$ versus applied tangential displacement $\overline{U}_{\mathrm{x}}$. Results are shown for the normal displacement $\overline{\delta} = 0$ and $\overline{\phi}_{\mathrm{n}} = \overline{\phi}_{\mathrm{t}} = 2$.

contact in Section 6.3, a sawtooth curve for $\overline{F}$ versus $\overline{U}_{\mathrm{x}}$ is observed due to the stick-slip motion. The evolution of the normal contact force $\overline{L}$ is also included in Fig. 6.6 (see the dashed blue line). Here, the negative value of $\overline{L}$ indicates tensile loading. This means that the summation of the attractive forces (with negative sign) on the interface is larger than the repulsive forces (with positive sign). By applying a larger $\overline{\delta}$ the solids are pushed harder against each other and the normal contact force $\overline{L}$ may become positive (compressive loading).

Figure 6.6 also presents the evolution of the contact area $\bar{A}$ during tangential loading, shown by the dotted red line. During the sticking stages, a reduction in $\bar{A}$ is observed with increasing $\overline{U}_{\mathrm{x}}$, a behaviour is refer to as “shear-peeling". Subsequently, at the onset of sliding where the slip instability occurs, the contact area abruptly increases and there is a reattachment at the interface. The cycle of area reduction → slip instability → reattachment persists for continued tangential displacement. The details of these events are examined in the following.

6.4.1. SHEAR–PEELING AND REATTACHMENT

Waters and Guduru [3] recorded images of the contact area evolution throughout their contact shearing experiments for a range of normal loads. Before the onset of sliding, these images demonstrated symmetric and asymmetric contact area reduction under tensile and compressive loading, respectively. After the onset of sliding, they could capture a partial reattachment under compressive loading. Here, simulations are performed with the aim of capturing these experimental features and to investigate whether the reattachment occurs also under tensile loading. Moreover, the role of friction on the evolution of contact area is studied.

Figure 6.7a shows the evolution of the contact area $\bar{A}$ versus the applied tangential displacement $\overline{U}_x$ at various normal loadings, tensile and compressive, and the ratio of the tangential-to-normal work of separation, $\phi_t/\phi_n = 1$ and 0.1. For the chosen parameters in this figure, $\overline{\delta} \gtrsim 0.2$ and $\overline{\delta} < 0.2$ represent the compressive and tensile loading, respectively. Moreover, $\phi_t/\phi_n = 1$ and 0.1 are employed in order to investigate the role of high and low friction, respectively, on the contact area evolution: Lowering the value of ϕ_t/ϕ_n, for example, resembles introducing lubricant into the interface.

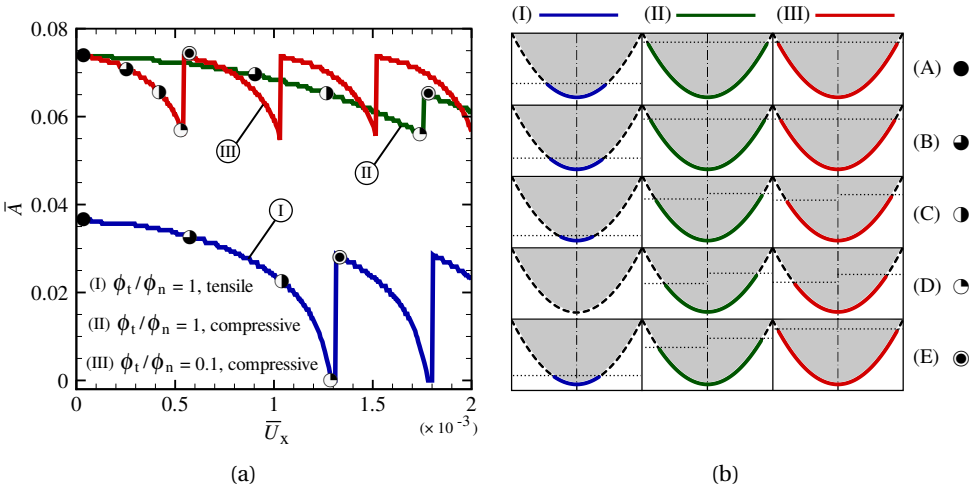

Figure 6.7: (a) Contact area $\bar{A}$ versus applied tangential displacement $\overline{U}_x$ for different normal loading and ratio of tangential-to-normal work of separation. (b) Snapshots (A–E) of the contact region during tangential loading for the three cases shown in (a). Snapshots are denoted by the same symbols in both (a) and (b). Note that in (b), contact regions are shown in the original configuration. The horizontal dotted lines are a visual aid to distinguish between symmetry and asymmetry of the contact area. Results are shown for $\overline{\phi}_n = 2$.

Snapshots of the contact region, labelled as A–E, are shown in Fig. 6.7b for

three cases in Fig. 6.7a at various values of the tangential displacement. These snapshots are denoted by the same symbols in both figures. In all cases, snapshot A is at $\overline{U}_x = 0$, B and C are during the shear-peeling stage, and D and E are before and after the first slip instability event. The following key features emerge from this figure:

- A → B: The contact area shrinks symmetrically. This symmetrical peeling is observed in all cases: tensile/compressive loading and low/high friction.
- B → C: Under tensile loading (case I), the contact area continues to shrink symmetrically. For compressive loading (case II and III), however, the contact area becomes asymmetric, with more peel occurring at the trailing edge of the contact than at the leading edge. The horizontal dotted lines are a visual aid to distinguish between symmetry and asymmetry of the contact area.
- C → D: Under tensile loading in case I, a full separation occurs during tangential loading at the onset of sliding. On the contrary, for compressive loading (case II and III), there is no full separation and contact area continues to shrink asymmetrically.
- D → E: As slip progresses within the contact area, slip instability occurs and immediately reattachment follows. Under tensile/compressive loading with high friction (case I and II), the reattachment occurs only partially. However, for the interface with low friction (case III), a full reattachment is observed (compare snapshots E and A).

The aforementioned features agree well with the experimental observations of Waters and Guduru [3]. Besides, two extra features are also captured compared to the experiments: First, the reattachment (D → E) was not observed for tensile loading (case I) in the experiments. As mentioned in [3], this is because the employed feedback loop could not correct the normal loading fast enough to maintain contact as the slip instability occurred. Second, for the chosen material and interface properties only a *partial* reattachment was observed in the experiments. However, the results here show that attaining a *full* reattachment is possible when friction is low (case III). In this case, as can be seen from the red line in Fig. 6.7a, the pre-sliding distance is small. Hence, the induced deformation in the solid during the sticking stage can be fully released as the slip instability occurs. Consequently, for the case of low friction, the initial configuration is re-attainable in the reattachment cycle.

6.4.2. LAWS OF AREA REDUCTION AND ONSET OF SLIDING

A common way of identifying the law of contact area reduction is to plot the contact area $\bar{A}$ as a function of the tangential contact force $\overline{F}$. To this end, the evolution of $\bar{A}$ versus $\overline{F}$ up to the onset of sliding for various normal displacements $\overline{\delta}$ is shown in Fig. 6.8a. For the chosen parameters in this figure, $\overline{\delta} \gtrsim 0.2$ and $\overline{\delta} < 0.2$

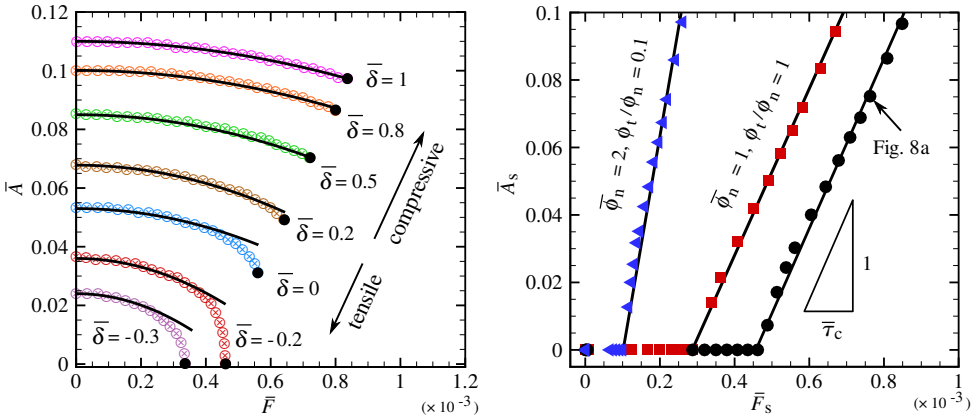

(a) $\overline{\phi}_n = 2,\ \phi_t/\phi_n = 1$ (b) $-1 \le \overline{\delta} \le 1$

Figure 6.8: (a) Evolution of the contact area $\bar{A}$ versus tangential contact force $\overline{F}$ for various normal displacements $\overline{\delta}$. Solid curves are fits using Eq. 6.8 [4]. The filled circles indicate contact area $\bar{A}_s$ at the maximum tangential contact force $\overline{F}_s$. (b) $\bar{A}_s$ versus $\overline{F}_s$ for the case shown in (a) along with cases for $\overline{\phi}_n = 1$, $\phi_t/\phi_n = 1$ and $\overline{\phi}_n = 2$, $\phi_t/\phi_n = 0.1$. Slopes of the solid lines in (b) represent the contact shear strength $\overline{\tau}_c$ [4].

represent the compressive and tensile loading, respectively. It is observed that for all $\overline{\delta}$, the initial contact area $\bar{A}_0 = \bar{A}$ ($\overline{U}_x = 0$) decreases until a maximum $\overline{F}$ is reached at the onset of sliding.

Recently, Sahli *et al.* [4] carried out sliding experiments for a range of compressive loadings. In their experiments, for both smooth and rough asperities, the reduction in the contact area was found to be well fitted by an empirical quadratic law of the form:

$$\bar{A} = \bar{A}_0 - \zeta\, \overline{F}^2, \tag{6.8}$$

with ζ being a fitting parameter. Here, this equation is fitted to the results for adhesive frictional contact of a smooth asperity with various normal displacements $\overline{\delta}$, see the solid curves in Fig. 6.8a. It is observed that a good agreement is obtained for compressive loading, similar to the experiments in [4]. For tensile loading, for which experimental data is not available, a deviation is found from the quadratic law of Eq. 6.8. It is concluded that under tensile loading, when the onset of sliding is approached, the rate of contact area reduction increases.

In Figure 6.8a, filled black circles indicate contact area $\bar{A}_s$ at the maximum tangential contact force $\overline{F}_s$ just before the onset of sliding, i.e. the static friction force. Figure 6.8b illustrates the data points $(\bar{A}_s, \bar{F}_s)$ related to various $\overline{\delta}$ for the case shown in Fig. 6.8a ($\overline{\phi}_n = 2$, $\phi_t/\phi_n = 1$) along with two other cases where $\overline{\phi}_n$ and ϕ_t/ϕ_n are independently varied. Interestingly, in all cases, the points marking the onset of sliding $(\bar{A}_s, \overline{F}_s)$ align well on a straight line. This shows that,

$$\overline{F}_s = \overline{\tau}_c \, \bar{A}_s + \overline{F}_{s,\,nc}, \tag{6.9}$$

with $\overline{\tau}_c$ and $\overline{F}_{s,\,nc}$ being the contact shear strength and the maximum sliding force without contact (i.e. without a surface area under repulsion), respectively.

The linear relation in Eq. 6.9 is in line with the so-called threshold law by Sahli *et al.* [4]. Since Sahli *et al.* [4] only considered compressive loading, they concluded that the straight line goes through the origin. Here, by considering also tensile loading, it is observed that in some cases $\bar{A}_s$ is zero at a finite value of tangential contact force due to the adhesive interactions at the interface. For example, in Fig. 6.8a, this is the case for the normal displacements $\overline{\delta} = -0.2$ and -0.3. This behaviour can be better captured by the proposed 'extended threshold law' (Eq. 6.9), choosing this name is inspired by the extended Amontons' law, which incorporates similarly an adhesive contribution.

Finally, Fig. 6.8b shows that the contact shear strength $\overline{\tau}_c$ and the sliding force when there is no repulsive surface area $\overline{F}_{s,\,nc}$ change with interface properties, namely $\overline{\phi}_n$ and ϕ_t/ϕ_n. The following key features are identified:

- Decreasing the normal work of separation decreases $\overline{F}_{s,\,nc}$, yet it has negligible effect on $\overline{\tau}_c$. This can be seen from Fig. 6.8b, by comparing the lines marked with black circles for $\overline{\phi}_n = 2$ and red squares for $\overline{\phi}_n = 1$. A way to reduce $\overline{\phi}_n$ is the immersion of the surface in ethanol or salt solution [18].

- Decreasing the ratio of tangential-to-normal work of separation results in smaller values of $\overline{F}_{s,\,nc}$ and $\overline{\tau}_c$. This is observed from Fig. 6.8b, by comparing the lines marked with black circles for $\phi_t/\phi_n = 1$ and blue triangles for $\phi_t/\phi_n = 0.1$ (in both cases $\overline{\phi}_n = 2$). The value of $\overline{\phi}_t$ can be reduced by introducing a lubricant into the interface.

6.5. CONCLUSIONS

A simple computational model is developed to study adhesive frictional contacts of elastically deformable solids under mixed-mode loading. The strength of the model lies in its capability of studying the variation of contact area and of the

friction force before and after the onset of sliding, under a compressive or tensile loading. The full range of conditions is difficult to be addressed experimentally.

The simulations are performed for an adhesive circular protrusion sliding against a rigid flat. The model can capture the features observed in the experiments by Waters and Guduru [3] and by Sahli *et al.* [4]:

- Under compressive loading, a tangential displacement, first induces the contact area to shrink symmetrically. As the applied tangential displacement increases more peel occurs at the trailing edge. Under tensile loading, on the contrary, the contact area continues to shrink symmetrically.
- Reduction in the contact area as a function of the tangential contact force is found to be well fitted by the empirical quadratic law reported in [4] for experimental results under compressive loading.
- There is a linear relation between the maximum tangential contact force at the onset of sliding and its corresponding contact area at various normal loadings.

In addition, the model can predict the following behaviours, not yet observed experimentally:

- With slip instabilities occurring during sliding, a cycle of contact area reduction and reattachment persists for continued tangential loading, even under tension. Whether the reattachment is partial or full depends on friction: The lower the friction, the more complete the reattachment.
- Under tensile loading the empirical quadratic law relating area to tangential force breaks down: There is a larger rate of contact area reduction when the onset of sliding is approached.
- Also under tensile loading a linear relation holds between the maximum tangential contact force at the onset of sliding and the corresponding contact area. However, under tensile loading, a full interface separation can take place at the onset of sliding with a non-zero tangential force: The contact area is under adhesive contact.

REFERENCES

[1] M. Khajeh Salehani, N. Irani, and L. Nicola, *Modelling adhesive contacts under mixed–mode loading*, Journal of the Mechanics and Physics of Solids, accepted for publication (2019).

[2] A. Savkoor and G. Briggs, *The effect of tangential force on the contact of elastic solids in adhesion,* Proceedings of the Royal Society of London A: Mathematical, Physical and Engineering Sciences **356**, 103 (1977).

[3] J. F. Waters and P. R. Guduru, *Mode-mixity-dependent adhesive contact of a sphere on a plane surface,* Proceedings of the Royal Society of London A: Mathematical, Physical and Engineering Sciences **466**, 1303 (2010).

[4] R. Sahli, G. Pallares, C. Ducottet, I. B. Ali, S. Al Akhrass, M. Guibert, and J. Scheibert, *Evolution of real contact area under shear and the value of static friction of soft materials,* Proceedings of the National Academy of Sciences **115**, 471 (2018).

[5] C. Thornton, *Interparticle sliding in the presence of adhesion,* Journal of Physics D: Applied Physics **24**, 1942 (1991).

[6] K. L. Johnson, *Adhesion and friction between a smooth elastic spherical asperity and a plane surface,* Proceedings of the Royal Society of London A: Mathematical, Physical and Engineering Sciences **453**, 163 (1997).

[7] S. Chen and T. Wang, *General solution to two-dimensional nonslipping JKR model with a pulling force in an arbitrary direction,* Journal of Colloid and Interface Science **302**, 363 (2006).

[8] M. Ciavarella, *Fracture mechanics simple calculations to explain small reduction of the real contact area under shear,* Facta Universitatis, Series: Mechanical Engineering **16**, 87 (2018).

[9] G. G. Adams, *Stick, partial slip and sliding in the plane strain micro contact of two elastic bodies,* Royal Society Open Science **1**, 140363 (2014).

[10] G.-Y. Huang and J.-F. Yan, *A mechanical model for the adhesive contact with local sliding induced by a tangential force,* Acta Mechanica Solida Sinica **30**, 369 (2017).

[11] J. C. Mergel, R. Sahli, J. Scheibert, and R. A. Sauer, *Continuum contact models for coupled adhesion and friction,* The Journal of Adhesion **0**, 1 (2018).

[12] A. Socoliuc, R. Bennewitz, E. Gnecco, and E. Meyer, *Transition from stick-slip to continuous sliding in atomic friction: entering a new regime of ultralow friction,* Physical Review Letters **92**, 134301 (2004).

[13] R. J. Dikken, B. J. Thijsse, and L. Nicola, *Friction of atomically stepped surfaces,* Physical Review B **95**, 104106 (2017).

[14] M. Khajeh Salehani, N. Irani, M. Müser, and L. Nicola, *Modelling coupled normal and tangential tractions in adhesive contacts,* Tribology International **124**, 93 (2018).

[15] J. P. McGarry, É. Ó. Máirtín, G. Parry, and G. E. Beltz, *Potential-based and non-potential-based cohesive zone formulations under mixed-mode separation and over-closure. part I: Theoretical analysis,* Journal of the Mechanics and Physics of Solids **63**, 336 (2014).

[16] S. Y. Krylov and J. W. Frenken, *The physics of atomic-scale friction: Basic considerations and open questions,* Physica Status Solidi (b) **251**, 711 (2014).

[17] E. Gnecco and E. Meyer, *Fundamentals of Friction and Wear on the Nanoscale* (Springer, 2015).

[18] J. Gao, W. Luedtke, D. Gourdon, M. Ruths, J. Israelachvili, and U. Landman, *Frictional forces and Amontons' law: from the molecular to the macroscopic scale,* The Journal of Physical Chemistry B **108**, 3410 (2004).

7

Conclusion

If you want a happy ending, that depends, of course,
on where you stop your story.

George Orson Welles

THE main objective of this thesis was to obtain a better understanding of adhesive contact and its frictional behaviour. To this end, a simple atomistically–inspired macro-scale model was developed in order to study smooth and rough contacts between elastically deformable bodies where adhesion and friction are simultaneously active at the interface.

In Chapter 2 a full description of the model is presented. There, the Green's function molecular dynamics (GFMD) technique is extended to explicitly describe the two solids in contact and their mixed-mode interface interactions. This extension includes an incremental iterative scheme, which is necessary to capture the contact area evolution as tangential tractions develop at the interface between the bodies under contact loading. Moreover, the interactions between surfaces are described through a coupled cohesive-zone model (CZM) implemented in the GFMD technique. Thereafter, the developed model is employed to thoroughly investigate the contact evolution under various practical conditions.

In Chapter 3 the non-adhesive contact between a rigid rough indenter and an incompressible elastic solid is studied. It is shown that for 1D smooth asperity (cylindrical) contacts, similar to 2D smooth asperity (Hertzian) cases, a linear relation can be obtained between contact area and reduced pressure only if the root-mean-square gradient (RMSG) is calculated over the actual contact area ($\bar{g}_r$), instead of the nominal contact area ($\bar{g}$). Furthermore, the assumption of linearity for random rough contacts is assessed where the proportionality factor is computed using both definitions of RMSG, κ and κ_r, in line and surface contacts. This leads to the following conclusions:

- For rough line (1D) contacts, only when the RMSG is calculated over the *actual* contact area a linear relation exists between the relative contact area and the reduced pressure, such that the proportionality factor $\kappa_r^{1D} \simeq 1.75$ is independent of Hurst exponent and reduced pressure.
- For rough surface (2D) contacts, both the values of κ^{2D} and κ_r^{2D} are negligibly dependent on Hurst exponent and reduced pressure.
- Based on the obtained values for the proportionality factor κ_r in 1D and 2D contacts, a single 1D-to-2D scaling factor $\kappa_r^{1D}/\kappa_r^{2D} \sim 0.9$ is found for both rough and smooth asperities.

In Chapter 4, the adhesive contact of a periodic array of smooth circular rigid asperities indenting into a flat deformable solid is studied. The aim of this study is to capture the consequences of the interplay between adhesion and friction during single mode normal loading. The main results of Chapter 4 are:

- For a given normal work of separation, the contact size increases by increasing friction. The dependency of contact size on friction is observed for various heights of the deformable solid.

- The interplay between adhesion and friction results in a decrease of the pull–off load. The decrease is maximum for a frictionless contact, as sliding is maximum. Increasing friction increases the pull-off load.

- The effect of adhesion and friction interplay on both the contact size and the pull-off load is strongest for highly adhesive contacts and materials with small Poisson's ratio.

- The adhesion and friction interplay can be neglected in all cases where relative sliding of the surfaces is small, i.e. when one of these three conditions hold: (1) friction is very large, (2) the material is incompressible, (3) contacts are closely spaced.

The adhesive contact of a self-affine rough rigid solid indenting an initially flat deformable solid is analysed in Chapter 5. This analysis leads to the following conclusions:

- The load-area relation is non-linear. Non-linearity is more pronounced for rough profiles with large Hurst exponent and/or small root-mean-square height.

- For small Hurst exponents the load-area relation depends on the small wavelengths cut-off used to described the roughness. In this case, non-linearity increases with increasing the small wavelength cut-off.

- Compressibility and friction can be neglected when investigating the load-area relation, since they affect it negligibly.

Contact problems that include also tangential loading are studied in Chapter 6. First, the model introduced in Chapter 2 is extended to approach contact problems under mixed-mode loading. To this end, an interface model is developed where the interface interactions between two bodies are described by sets of "springs", mimicking interatomic interactions. Then, frictional sliding of the adhesive contact of a circular smooth punch against a flat rigid substrate, under tension and compression, is investigated. The model can capture the features observed experimentally:

- Under compressive loading, a tangential displacement, first induces the contact area to shrink symmetrically. As the applied tangential displacement increases more peel occurs at the trailing edge. Under tensile loading, on the contrary, the contact area continues to shrink symmetrically.
- Reduction in the contact area as a function of the tangential contact force is found to be well fitted by the empirical quadratic law reported from experimental results under compressive loading.
- There is a linear relation between the maximum tangential contact force at the onset of sliding and its corresponding contact area at various normal loadings.

In addition, the model can predict the following behaviours, not yet observed experimentally:

- With slip instabilities occurring during sliding, a cycle of contact area reduction and reattachment persists for continued tangential loading, even under tension. Whether the reattachment is partial or full depends on friction: The lower the friction, the more complete the reattachment.
- Under tensile loading the empirical quadratic law relating area to tangential force breaks down: There is a larger rate of contact area reduction when the onset of sliding is approached.
- Also under tensile loading a linear relation holds between the maximum tangential contact force at the onset of sliding and the corresponding contact area. However, under tensile loading, a full interface separation can take place at the onset of sliding with a non-zero tangential force: The contact area is under adhesive contact.

CURRICULUM VITÆ

Mohsen KHAJEH SALEHANI

30-07-1990 Born in Tehran, Iran.

EDUCATION

2004–2008 High School Diploma in Mathematics & Physics

2008–2012 B.Sc. in Mechanical Engineering (Cum-Laude)
Sharif University of Technology
Thesis: Finite element analysis of internal crack formation in extrusion processes

2012–2014 M.Sc. in Computational Solid Mechanics (Cum-Laude)
Sharif University of Technology
Thesis: Crystal plasticity simulation of orientation evolution in sheet metal forming

2015–2019 Ph.D. in Computational Mechanics and Materials Science
Delft University of Technology
Thesis: Modelling adhesion and friction in contact problems

LIST OF PUBLICATIONS

4. **M. Khajeh Salehani**, **J. S. van Dokkum**, **N. Irani**, **L. Nicola**, *On the load–area relation in rough adhesive contacts*, Submitted for publication (2019).

3. **M. Khajeh Salehani**, **N. Irani**, **L. Nicola**, *Modelling adhesive contacts under mixed–mode loading*, Journal of the Mechanics and Physics of Solids, accepted for publication (2019).

2. **J. S. van Dokkum**, **M. Khajeh Salehani**, **N. Irani**, **L. Nicola**, *On the proportionality between area and load in line contacts*, Tribology Letters **66**, 115 (2018).

1. **M. Khajeh Salehani**, **N. Irani**, **M. Müser**, **L. Nicola**, *Modelling coupled normal and tangential tractions in adhesive contacts*, Tribology International **124**, 93 (2018).